

Study of Various Detection Mechanisms for Photoacoustic Imaging

by

Jasmine Yi Jie Chan

A thesis
presented to the University of Waterloo
in fulfillment of the
thesis requirement for the degree of
Master of Applied Science
in
System Design Engineering

Waterloo, Ontario, Canada, 2020

©Jasmine Yi Jie Chan 2020

AUTHOR'S DECLARATION

This thesis consists of material all of which I authored or co-authored: see Statement of Contributions included in the thesis. This is a true copy of the thesis, including any required final revisions, as accepted by my examiners.

I understand that my thesis may be made electronically available to the public.

STATEMENTS OF CONTRIBUTION

This thesis consists of a co-authored paper where I was the primary author. The co-authors have provided many insightful information and guidance in the writing and editing of this paper.

1. *Photoacoustic Imaging with Capacitive Micromachined Ultrasound Transducers : Principles and Developments*

This work is presented in Chapters 2, 3 and 7 of this thesis [1].

J. Chan, Z. Zheng, K. Bell, M. Le, P. H. Reza, and J. T. W. Yeow, “Photoacoustic Imaging with Capacitive Micromachined Ultrasound Transducers : Principles and Developments,” *Sensors (Switzerland)*, vol. 19, no. 3617, 2019

Abstract

Photoacoustic imaging (PAI) is a developing imaging technique that has been researched for several clinical applications including oncology, neurology, dermatology and ophthalmology. PAI combines the benefits of pure optical and acoustic imaging to attain optical absorption contrast images. There are three different modalities in photoacoustic imaging which are categorized according to the type of image reconstruction and the focus. Photoacoustic computed tomography (PACT) uses reconstruction-based image formation while photoacoustic microscopy (PAM) uses focused-based image formation. Photoacoustic microscopy can be further divided into optical-focused imaging, optical-resolution photoacoustic microscopy (OR-PAM) and acoustic-focused imaging, acoustic resolution photoacoustic microscopy (AR-PAM). The two essential components in the photoacoustic imaging system are the excitation laser, which is typically implemented as a pulsed laser, and the detector. Various detection mechanisms have been investigated for photoacoustic imaging, ranging from contact mode physical sensors to non-contact forms of detection. In this research project, photoacoustic imaging with a piezoelectric transducer and a novel non-contact detection mechanism, photoacoustic remote sensing (PARS) were studied for optical-resolution photoacoustic microscopy, OR-PAM applications. Conventional photoacoustic imaging uses a piezoelectric transducer to pick up the pressure induced by the photoacoustic effect. PARS system, on the other hand, captures the changes in the elasto-optical refractive index modulation caused by the photoacoustic initial pressure. The photoacoustic signals can be detected in two modes, transmission and reflection modes. When the excitation laser hits the sample, the photoacoustic signals are generated in different directions. In transmission mode, photoacoustic signals are detected below the sample while reflection mode is the sensing of photoacoustic signals that have bounced off the sample. A 2.25 MHz piezoelectric transducer was used in transmission mode to image carbon fibers network. For the PARS system, the piezoelectric transducer was replaced with a 637 nm continuous-wave laser. The continuous-wave detection laser was co-focused and co-scanned with an excitation laser to image the same carbon fiber networks in reflection mode.

The second objective of this research project focuses on the preliminary investigation of a micro-electro-mechanical system device, capacitive micromachined ultrasound transducers (CMUTs) for PAI applications. In comparison with conventional piezoelectric transducer, CMUTs generally have a larger bandwidth which will in turn attribute to a better axial resolution for applications such as PAM imaging.

Furthermore, unlike piezoelectric transducer, CMUTs have a similar acoustic impedance as tissue. Therefore, there is no need for an additional matching layer. A 3.4 MHz CMUT fabricated with nitride-to-oxide wafer bonding technology was analyzed and characterized for PAI in this research project.

Acknowledgements

This thesis could not have been completed without the help of many individuals. First and foremost, I would like to express my deepest appreciation and gratitude to both my supervisors, Prof John T.W. Yeow and Prof Parsin Hajireza for the opportunity given to work in their labs. Under both of their supervision, I have gained valuable insight and knowledge during this journey. It was an honor to work with both professors as it has broadened my horizon in the field of microelectromechanical systems (MEMS) devices and optics. Thank you for supporting me financially and providing me with all the necessary resources to aid me in completing my project. With both supervisors' unwavering enthusiasm for engineering, I was well guided on the path while working on this project. I would to thank Prof Eihab Abdel-Rahman and Prof Mustafa Yavuz for agreeing to be my thesis readers amidst their busy schedule.

I would also like to thank my colleagues from the Advanced Micro-/Nano- Devices Lab (AMNDL) and the Photomedicine Labs who has worked with me since the start of my journey in this project. It was a pleasure to be working alongside with them. Their constant beneficial feedbacks and early insights has aided me in my enhanced my knowledge in this area of photoacoustic imaging and MEMS. They have left a great impact in my life and the memories created in the labs will deeply engraved in my memory. Thank you all for making a foreign country feels like home, I am indebted to all of you. A special mention to Joe who is my mentor, thank you for being so patient to assist me and encourage me when my morale is getting low. I am also grateful to Layla who has been putting in a lot of time and effort in aiding me with my photoacoustic experiment. Without your help in the alignment of the optical set-up and photoacoustic imaging of the carbon fiber, I would not have been able to get my experiment done.

Lastly, I would like to thank my family who have always been there for me. It was not an easy decision to support me to study abroad, especially a country so far away. However, I am glad all of you still supported me emotionally, morally and financially. Thank you for listening to my problems despite not being able to relate to most of the engineering concepts. All of you are my pillar of support, who constantly give me your unconditional love and support. There is no word that can fully express my gratitude; thus, I will end it with a – thank you.

Table of Contents

AUTHOR'S DECLARATION	ii
STATEMENTS OF CONTRIBUTION	iii
Abstract	iv
Acknowledgements	vi
List of Figures	ix
List of Tables	xii
Chapter 1 Introduction.....	1
1.1 Motivation	1
1.2 Thesis Outline.....	3
Chapter 2 Background.....	4
2.1 Principle of Operation	6
2.2 Photoacoustic Modalities.....	7
2.2.1 Photoacoustic Computed Tomography	7
2.2.2 Photoacoustic Microscopy.....	8
2.3 Detectors Used in the Different PAI Modalities	9
Chapter 3 Detection mechanism for Photoacoustic Imaging	12
3.1 Contact-based Detection Technique.....	12
3.1.1 Fabry-Perot Interferometer.....	13
3.1.2 Micro Ring Resonator	14
3.1.3 Piezoelectric Transducer	15
3.1.4 Capacitive Micromachined Ultrasound Transducer	17
3.1.5 Discussion of the Physical Sensors	25
3.2 Non-contact-based Detection Technique.....	26
3.2.1 Interferometry	26
3.2.2 Photoacoustic Remote Sensing.....	28
3.3 Summary	31
Chapter 4 Optical Resolution Photoacoustic Microscopy Imaging Experiment	32
4.1 Receive sensitivity of Piezoelectric Transducer.....	32
4.2 Photoacoustic Imaging	34
Chapter 5 CMUT Modeling	38

5.1 Working Principle of Capacitive Micromachined Ultrasound Transducers	39
5.1.1 Numerical Analysis.....	39
5.1.2 Finite Element Analysis.....	47
5.2 Fabrication	50
5.2.1 Surface Micromachining.....	50
5.2.2 Wafer Bonding.....	51
Chapter 6 Testing and Characterization of Capacitive Micromachined Ultrasound Transducers	53
6.1 Parameters of Capacitive Micromachined Ultrasound Transducers	53
6.2 Characterization of Electrical Impedance	54
6.3 Characterization of Receive Sensitivity	56
6.4 Summary	60
Chapter 7 Summary and Future Work	61
7.1 Summary	61
7.2 Future Work.....	61
7.2.1 Industrialization of Capacitive Micromachined Ultrasound Transducer for Photoacoustic Imaging	61
7.2.2 Challenges and Prospects of Using Capacitive Micromachined Ultrasound Transducer for Photoacoustic Imaging.....	62
Bibliography	64

List of Figures

Figure 2.1 Absorption coefficient of various endogenous contrast at different wavelength [41].	6
Figure 2.2 Experimental set-up of (a) OR-PAM (b) AR-PAM (c) PACT [38], [68].	10
Figure 3.1 The working principle of FPI [2]. (b) Experimental set-up of OR-PAM imaging with GLAD nanostructured FPI [77].	14
Figure 3.2 (a) Schematic diagram of a micro ring resonator. (b) Experimental set-up of PAM with transparent MRR used in [4].	15
Figure 3.3 Schematic of the OR-PAM system. a: Condenser lens; b: pinhole; c: microscope objective; d: ultrasonic transducer; e: correcting lens; f: isosceles prism; g: acoustic lens; h: silicon oil [94].	16
Figure 3.4 (a) Capacitive micromachined ultrasound transducers (CMUT) transmission mode; (b) CMUT receiving mode.	17
Figure 3.5 (a) Model of the chicken breast phantom, (b) ultrasonic imaging, (c) PAI, and (d) a combination of photoacoustic and ultrasonic imaging [10]; (e) working principle of top orthogonal to bottom electrode TOBE) [12].	20
Figure 3.6 (a) Optical absorption of silicon under different wavelength and (b) structure of optically transparent CMUT, (c) imaging of mouse brain using the different frequencies of the CMUT, (d) interlaced CMUT, (e) multi-band CMUT, (f) monolithic multiband CMUT with five frequencies.	22
Figure 3.7 Timeline of CMUT designs for PAI endoscopes [76]–[79]; (a) inward-looking cylindrical transducer, (b) 9F MicroLinear CMUT ICE catheter; (c) miniature needle-shaped CMUT (d) integrated ring CMUT array.	24
Figure 3.8 Schematic of the experimental set-up [123].	27
Figure 3.9 Diagram of the PARS mechanism. (a) If a refractive index profile $n(x)$ exists at the boundary of an absorbing media having a refractive index n_1 , a DC reflection of a probe beam is expected before pulsed excitation occurs ($t=0^-$). (b) The excitation beam has been absorbed ($t=0^+$), and thermoelastic excitation of the absorber generates an initial pressure profile $p(x)$. This, in turn, perturbs the existing refractive index by δn , which produces an AC modulation in the reflected probe beam proportional to the absorption. Note that the DC component is not shown in this figure for simplicity. (c, d) If there is no existing refractive index step, then the small δn modulation generated by the absorption of the excitation beam creates a negligible AC signal variation (not shown) [7].	28

Figure 3.10 Experimental setup. PARS microscopy with 532-nm excitation and 1310-nm integration beams. BC, beam combiner; GM, galvanometer mirror; L, lens; OL, objective lens; PBS, polarized beam splitter; PD, photodiode; QWP, quarter-wave plate; SMF, single-mode fiber.....	29
Figure 3.11 In vivo en-face mouse ear images. (a) PARS images using two-axis lateral mechanical scanning. (b) Larger field of view images using mechanical scanning as well as a zoomed in image of both capillary beds and larger blood vessels using fast scanning mirror	30
Figure 4.1 A schematic of the experimental set-up for receive sensitivity.	32
Figure 4.2 Graph of time response of piezoelectric transducer as the receiver.....	33
Figure 4.3 Graph of frequency spectrum of piezoelectric transducer as the receiver.	33
Figure 5.1 Deflection of the CMUT with respect to its radial position when only atmospheric pressure is applied.	40
Figure 5.2 Mass spring-damper model of CMUT.....	41
Figure 5.3 The normalized force against the normalized distance of the spring force and electrostatic force.	42
Figure 5.4 Stable and unstable roots of displacement under different bias voltages	45
Figure 5.5 CMUT's small-signal circuit model $\mathbf{Z_p}$ is the plate impedance which comprise of the equivalent spring constant, \mathbf{k} and the mass, \mathbf{m} . $\mathbf{Z_m}$ is the medium impedance which consists of the resistance, $\mathbf{R_m}$ and the reactance, $\mathbf{X_m}$. In transit mode, $\mathbf{F_{source}} = \mathbf{0}$ while in receive mode, $\mathbf{V_{source}} = \mathbf{0}$	46
Figure 5.6 2D model of CMUT used in COMSOL	48
Figure 5.7 Frequency spectrum of CMUT operating in air under a bias voltage of 30V	48
Figure 5.8 Frequency spectrum of CMUT operating in immersion under a bias voltage of 30V	49
Figure 5.9 Displacement of CMUT membrane under different bias voltage using numerical and finite element analysis	49
Figure 5.10 Process flow of fabricating CMUTs with surface micromachining [130].....	50
Figure 5.11 Process flow of fabricating CMUTs with wafer bonding [130]	51
Figure 6.1 Diagram of CMUT used in the experiments.....	53
Figure 6.2 Schematic of the experimental set-up for characterization of electrical impedance	54
Figure 6.3 The electrical impedance of CMUT-R in (a) magnitude and (b) phase	55
Figure 6.4 (a) Circuit and (b) Experimental set-up of the transmission test	56
Figure 6.5 Graph of Time response of CMUT-T in transmission.....	57

Figure 6.6 Frequency spectrum of CMUT-T in transmission mode	57
Figure 6.7 Circuit set-up of CMUT-R.....	58
Figure 6.8 Time response of CMUT-R in receiving mode.....	59
Figure 6.9 Frequency Response of CMUT-R in receive mode	59

List of Tables

Table 1 The lateral resolution, penetration depth, detector center frequency, and applications for the different photoacoustic imaging (PAI) modalities.....	11
Table 2 The performance of different acoustic detectors along with their advantages and disadvantages in PAI applications.	25
Table 3 Comparison table between the piezoelectric transducer and PARS.	37
Table 4 Parameters used in modeling	48
Table 5 Parameters of fabricated CMUTs	53
Table 6 Comparison of CMUTs' center frequency and bandwidth from theoretical and experimental results	60

Chapter 1

Introduction

1.1 Motivation

Photoacoustic imaging (PAI) is an emerging imaging technique that bridges the gap between pure optical and acoustic techniques to provide images with optical absorption contrast by detecting the ultrasonic wave. The two key components that have allowed PAI to attain high-quality images at deep penetration depths are the photoacoustic signal generator, which is typically implemented as a pulsed laser and the detector to receive the generated acoustic signals. Over the years, several forms of photoacoustic signal detection methods have been developed. They can be classified into contact-based detection, which usually requires a physical sensor and non-contact-based detection. Many types of sensors have been explored as a detector for the PAI including Fabry–Perot interferometers (FPIs) [1], [2], micro ring resonators (MRRs) [3]–[5], piezoelectric transducers [6], and capacitive micromachined ultrasound transducers (CMUTs). Recently, a new PAI imaging method that does not require a physical sensor for detection and instead uses a secondary continuous laser beam to detect the photoacoustic signals was introduced. This imaging technique is known as photoacoustic remote sensing (PARS) [7], [8] and is currently further developed by our group at the Photomedicine Labs.

There are two objectives in this research project. The main aim of this research project is to study the various detection mechanism for PAI. Optical resolution photoacoustic microscopy (OR-PAM) imaging of carbon fibers was investigated with piezoelectric transducers and PARS. The secondary goal of this research project is to do a preliminary study on using a nitride-to-oxide wafer-bonded CMUTs for PAI. The fabrication technique of CMUTs has given it an edge over the other physical sensors. Firstly, CMUTs can be easily fabricated into given shapes and sizes to fit the design specifications. Moreover, they can be made into an array to increase the imaging speed and reduce motion artifacts. With a fabrication technique that is similar to complementary metal-oxide-semiconductor (CMOS), CMUTs can be integrated with electronics to reduce the parasitic capacitance and improve the signal to noise ratio. The numerous benefits of CMUTs have enticed researchers to develop it for various PAI purposes such as photoacoustic computed tomography (PACT) and photoacoustic endoscopy applications. For PACT applications, the main areas of research are in designing two-dimensional array [9]–[12], transparent [13]–[15], and multi-frequency CMUTs [16]–

[18]. Moving from the table top approach to endoscopes, some of the different configurations that are being investigated are phased [19], [20] and ring arrays [21], [22].

In 2017, our group at the Advanced Micro-/Nano- Devices Lab (AMNDL), presented a novel fabrication technique that uses silicon nitride as the membrane for wafer bonding. This fabrication technique has many advantages including lower fabrication cost and the flexibility to design membrane with different thickness [23]. In this work, a nitride-to-oxide wafer-bonded CMUTs was characterized and studied for PAI applications.

1.2 Thesis Outline

This thesis composed of seven chapters and is organized as follows.

- Chapter 2 introduces the fundamentals of optical and acoustic imaging and how PAI uses the concept of both imaging techniques to achieve optical absorption contrast images. The working principle and the different PAI modalities are also covered in this chapter.
- In Chapter 3, the operating idea along with the advantages and disadvantages of the different potential detection mechanisms of OR-PAM is discussed. This chapter also reviews the current state-of-the-art research of CMUTs for PAI application.
- Chapter 4 presents the PAI images and results of carbon fiber attained with a piezoelectric transducer and PARS system. The experimental data such as the lateral resolution and SNR were also analyzed.
- Chapter 5 further elaborates on the guiding principle and modeling of CMUTs with mathematical equations finite element analysis.
- In Chapter 6, characterization results of a CMUT fabricated with the nitride-to-oxide wafer-bonding technique are shown. The CMUT was characterized in the air using the vector network analyzer and parameters such as receive sensitivity were attained in oil immersion experiments.
- Finally, the thesis concludes in Chapter 7 with a summary and the potential future work.

Chapter 2

Background

Photoacoustic imaging (PAI) is a developing imaging technique researched for various clinical applications, including oncology [24], neurology [25]–[27], dermatology [28], [29], and ophthalmology [30]. The strength of PAI lies in its ability to bridge the gap between pure optical and acoustic imaging henceforth producing optical absorption-based images. Depending on the type of photoacoustic modality, PAI is able to achieve resolution of submicrometer and reach penetration depth that is as deep as several centimeters. The working principle of optical imaging methods is mainly governed by the scattering and absorption of photons, which can be categorized into four regimes. The ballistic regime is the region within the mean free path where the photons have not gone through any significant scattering. One example of an imaging system in this regime is confocal microscopy. In the quasi-ballistic regime, the region between the mean free path to the transport mean free path, the photons sustain minimal scattering. Nevertheless, this has a negligible impact on the photon's memory of the original path. Just below the quasi-ballistic regime is the quasi-diffusive regime. In this regime, the photons are subjected to much scattering such that the spatial and temporal coherence is degraded. Beyond 10 times the transport mean free path is the diffusive regime. The photons in this regime have a negligible recollection of the original path [31]. The spatial and temporal coherence is completely lost in this regime. For biological tissue, the mean free path is on the order of 0.1 mm while the optical transport mean free path is the order of 1 mm [31].

On the other hand, acoustic imaging makes use of the acoustic wave to penetrate deeper than the optical imaging. Imaging is done based on acoustic contrast mismatch, which, in the case of biomedical imaging is related to the mechanical properties of soft tissues [32]. As acoustic impedance is not encoded with molecular information, therefore acoustic imaging is unsuited for monitoring molecular activities such as the oxygenation level in hemoglobin [33]. Moreover, there is a trade-off between the penetration depth and the resolution where a high-resolution image commonly yields a low penetration depth and vice versa. This trade-off exists because the resolution produced by the acoustic imaging is dependent on the frequency of the signal. A shorter pulse length is usually desirable as it gives a higher image resolution. However, with high frequency comes high ultrasonic attenuation [32]–[34]. Consequently, it restricts the acoustic wave from penetrating deeper into the tissue.

Unlike acoustic imaging, PAI is able to take advantage of the optical contrast to provide histological, functional and metabolic imaging [35]. Besides, in comparison to optical imaging, PAI does not need to take into account the scattering of the returning light and instead relies on the acoustic wave to form the image. This allows the PAI to produce optical absorption contrast images that cover beyond the quasi-ballistic regime. By detecting acoustic waves instead of photons, PAI has a depth to resolution ratio of 2 orders of magnitude higher than the common optical imaging methods [36]–[38]. Furthermore, PAI is very sensitive to small changes in the optical absorption variation and can fully reflect these changes on the amplitude of the photoacoustic signal [35]. This linear relationship between the signal and the optical absorption permits linear spectral unmixing for multiplex and functional imaging [33].

Employing the idea that every biological cell and tissue have different optical absorption coefficients, an appropriate wavelength can be selected for the specific target. Hemoglobin is one of the strongest optical absorbers in the visible light range [33], [39]. When a tumor develops in the body, the amount of blood flow in that region tends to be higher as more blood vessels grow to provide cancer cells with oxygen and nutrients. This is known as angiogenesis. With PAI, a specific wavelength, such as 532 nm, can be used to track hemoglobin. Thus, areas with high blood flow can be detected without exogenous labels [39]. The ability to image hemoglobin will be immensely useful in aiding clinicians in the advancement of cancer studies. Other examples of endogenous contrast include melanin, lipids, and DNA/RNA [40]. The absorption coefficient of some of the endogenous contrast at different wavelengths is shown in figure 2.1. Exogenous contrast can be introduced to target specific cells or tissue when endogenous contrast is unable to produce a substantial signal. With a large variety of exogenous contrast available, selecting an exogenous contrast with a high absorption coefficient at the specified laser wavelength can improve the imaging sensitivity. Examples of exogenous contrast used in PAI are organic dyes, fluorescent proteins, and nanoparticles [40].

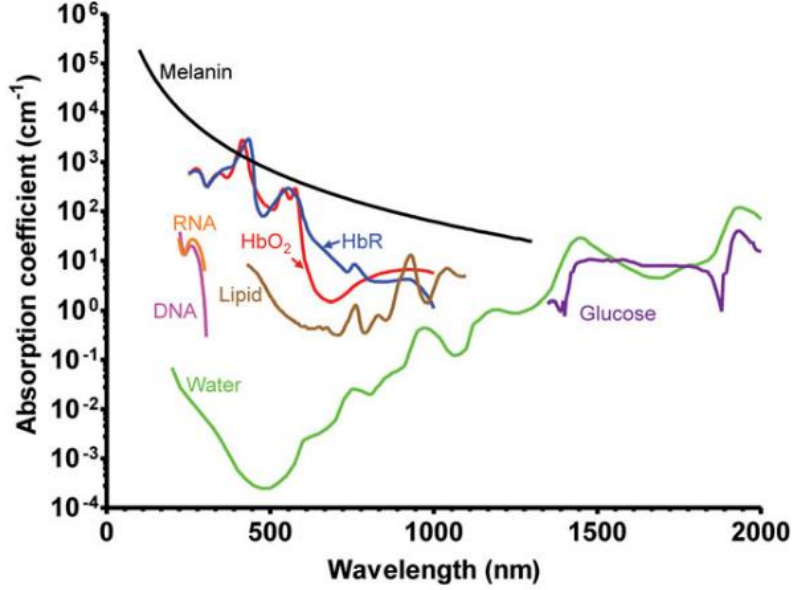


Figure 2.1 Absorption coefficient of various endogenous contrast at different wavelength [41].

2.1 Principle of Operation

In PAI for biomedical application, a short pulse laser, usually in the visible to near-infrared of the electromagnetic spectrum is first illuminated onto the tissue. The tissue then experiences thermoelastic expansion where it heats up and expands. During this brief expansion, the pressure within the tissue increases, thereby generating ultrasound waves that are picked up by the detector. The detector converts this ultrasound wave into a signal which is amplified and stored into a data acquisition card for image reconstruction [31].

The key phenomenon for photoacoustic imaging is the local pressure rise P_0 inside the tissue [37]. The two important parameters for photoacoustic imaging are the thermal relaxation time and the stress relaxation time. When a laser hits a tissue, the volume expansion can be expressed as

$$\frac{dV}{V} = -\kappa p + \beta T \quad (2.1)$$

where $\frac{dV}{V}$ is the fractional volume expansion of the heated region, κ is the isothermal compressibility, p is the change in pressure and T is the change in temperature. If the duration of the laser pulse is

smaller than the thermal relation time and the stress relaxation time, the change in volume will be negligible and the initial pressure, P_0 can be derived.

$$P_0 = \frac{\beta T}{\kappa} \quad (2.2)$$

The change in local temperature can be expressed as

$$T = \frac{Ae}{\rho Cv} \quad (2.3)$$

where Ae is the specific optical energy deposition, ρ is the mass density and Cv is the specific heat in constant volume. By substituting the local temperature (2.3) into (2.2), we will get

$$P_0 = \frac{\beta Ae}{\kappa \rho Cv} = \Gamma Ae \quad (2.4)$$

where $\Gamma = \frac{\beta}{\kappa \rho Cv}$ is the Grueneisen parameter. Since Ae is proportional to the local optical fluence in the case of single-photon optical absorption, equation (2.4) can be rewritten as follows.

$$P_0 = \Gamma F \mu_a \quad (2.5)$$

where μ_a is the optical absorption coefficient. Although Γ is dependent on tissue type, it is generally considered a constant. Thus, μ_a can be found with P_0 and F known.

2.2 Photoacoustic Modalities

PAI can be split into two main categories based on the way images are formed. Photoacoustic computed tomography (PACT) uses reconstruction-based image formation, while photoacoustic microscopy (PAM) uses focused-based image formation.

2.2.1 Photoacoustic Computed Tomography

In PACT, an unfocused optical beam is used to excite an area of the material, and an array of sensors measure the generated ultrasound waves in the various positions [35]. PACT has reportedly been able to penetrate as deep as 7 cm into the tissue, but consequently, it may only deliver a lateral resolution of hundreds of micrometers [42], [43]. With different algorithms available, time reversal and back-projection methods are the two most popular techniques for image reconstruction. Time reversal is a time iterative reconstruction algorithm and as its name suggests, works by re-emitting the wave in a time-reversed manner via an acoustic propagation model [33], [44]. Because of the intensive computation required to obtain the image, the time-reversal method has not been applied for practical

use [33], [37], [45]. The back-projection method, like time reversal, employs the knowledge of the speed of sound in the medium to resolve the ultrasound waves and back project them to form the image [33]. This method is similar to the delay and sum beamforming method used in ultrasound imaging. Since the back-projection method requires lesser time to form an image, it is more applicable for real-time imaging [46].

PACT can be used for many applications ranging from microscopic to macroscopic imaging [42]. As it receives the signal from multiple elements, PACT can provide a larger field of view (FOV) with a single shot in the diffusive regime. Therefore, it can be used to image the whole body of small animals [43] and has also been evaluated for uses in neurology [25], [27], [47], [48], cardiology [49], and label-free breast cancer studies [50]. However, imaging such a large field of view requires a large acceptance angle to receive signals from multiple locations of the same object [35]. With such a large dataset, the imaging speed will be dependent on the data acquisition system [36].

2.2.2 Photoacoustic Microscopy

Unlike PACT, PAM uses a focused beam and detects using a single element that is raster-scanned about the sample [41]. The signal which is dependent on the optical energy deposited is resolved with respect to the acoustic axis, and the envelope of this recorded time-domain signal is extracted to form the image [35]. PAM is generally used for applications that require high-resolution images rather than deep penetration depth like the studying of the microenvironment of diseases using small animals [51]. PAM can be further divided into two imaging methods depending on whether the generated photoacoustic signal is more optically or acoustically focused. Optical resolution photoacoustic microscopy (OR-PAM) takes advantage of the optical focus to obtain a high lateral resolution, while acoustic resolution photoacoustic microscopy (AR-PAM) utilizes acoustic focusing to image at depths greater than the transport mean free path of the excitation pulse.

Acoustic Resolution Photoacoustic Microscopy

As mentioned previously, AR-PAM has a tighter acoustic focus for imaging. Since the acoustic focus is limited by the acoustic diffraction limit rather than the optical diffraction limit, the lateral resolution attainable by AR-PAM is only tens of micrometers [52]. Conversely, acoustic waves scatter less than

visible photons in scattering media. Hence, AR-PAM has been demonstrated to penetration depths of up to 11 mm [53], which is 10 times more than OR-PAM.

The maximum permissible exposure (MPE) allowed by the American National Standard Institute (ANSI) for nanosecond pulsed wavelengths between 400 to 700 nm in human tissue is 20 mJ/cm² [54]. As a larger area is illuminated, AR-PAM has a higher energy allowable limit than OR-PAM [36]. This allows more photons to reach deeper into the tissue, producing higher quality images at deeper penetration depths. Moreover, AR-PAM is able to maintain the same contrast for a broad range of imaging resolution [55]. These advantages make AR-PAM a good imaging modality to be explored for different applications such as imaging sentinel lymph nodes [53], [56] detecting cystography [57], and gastrointestinal imaging [58].

Optical Resolution Photoacoustic Microscopy

OR-PAM, on the other hand, emphasizes more on the photons rather than the acoustic waves. In OR-PAM, the optical focus of the excitation beam is tightened to form the image. The lateral resolution is limited by the optical diffraction of the focused laser onto the tissue [59], [60]. Indeed, OR-PAM can produce images with higher lateral resolution than AR-PAM, but its penetration depth is restricted by the optical transport mean free path, which for biological tissue is ~1 mm [59].

Making use of its optical focus, OR-PAM can be used for label-free imaging within the optical quasi-ballistic regime. The high resolution that it can achieve makes it suitable for imaging small targets ranging from a capillary vein, which can be less than 10 μ m to even smaller targets like cells [35], [41], [52]. OR-PAM has also been investigated for a broad range of applications to understand diseases and the biological environments in the eyes [61], [62], skin [63], and brain [64].

2.3 Detectors Used in the Different PAI Modalities

There are three detection geometries used in PACT applications namely, planar, cylindrical, and spherical. Planar view PACT systems usually use two-dimensional (2D) planar, phased, or linear arrays for imaging, while cylindrical view PACT systems detect with ring arrays [65]. Spherical view PACT systems have been used for imaging with arc-shaped transducer array [66] and hemispherical transducer

array [49]. The axial resolution of all three PACT systems is determined by the bandwidth of the detector, while their lateral resolution is dependent on their detection geometries [38]. Similarly, the axial resolution of PAM is also determined by the bandwidth of the detector however, the lateral resolution is based on the acoustic wavelength for AR-PAM and optical wavelength for OR-PAM [40]. OR-PAM mainly relies on the optical focus to attain a high-resolution image while in AR-PAM, the laser beam is weakly focused and a focused transducer is used [67]. Nonetheless, higher frequency and sensitivity detectors are needed in both PAM modalities to enable them for the real-world clinical and pre-clinical applications. The lateral resolution and penetration depth that various PAI modalities can deliver, along with their main area of applications are presented in Table 1. The experimental set-up of the PACT and PAM systems are shown in figure 2.2.

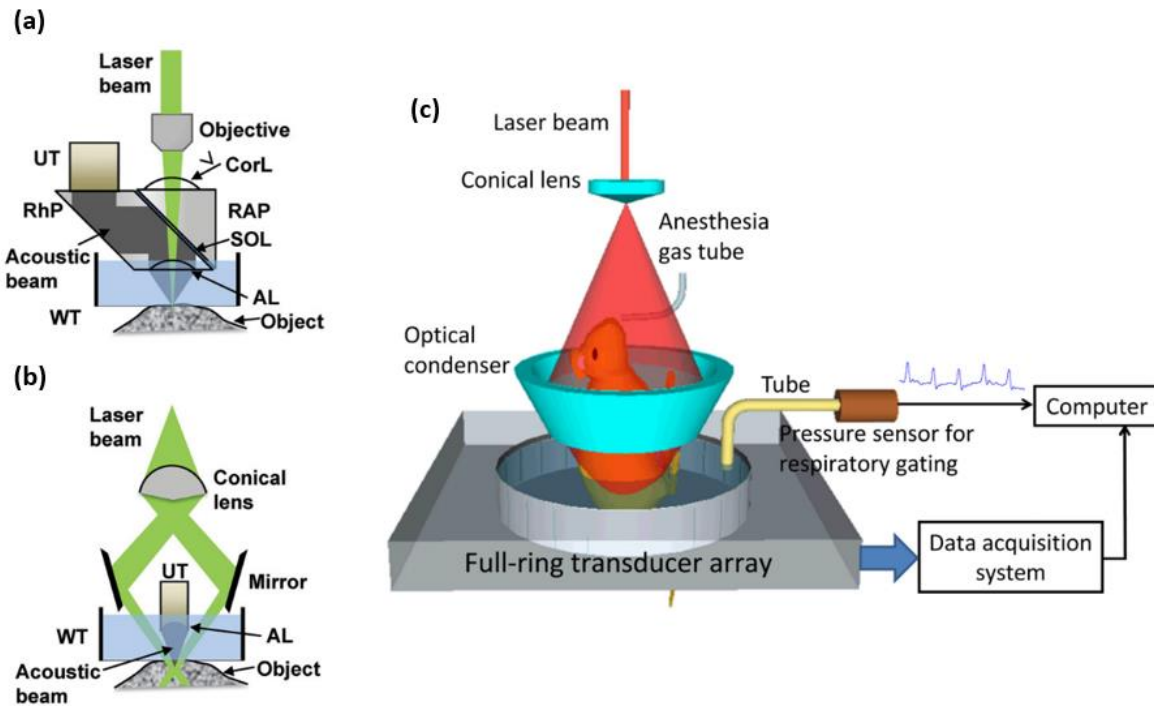


Figure 2.2 Experimental set-up of (a) OR-PAM (b) AR-PAM (c) PACT [38], [68].

Table 1 The lateral resolution, penetration depth, detector center frequency, and applications for the different photoacoustic imaging (PAI) modalities.

PAI Modalities	Typical Lateral Resolution Range	Typical Penetration Depth	Detector Center Frequency	Application
Photoacoustic computed tomography (PACT) [25], [27], [42], [43], [48], [49]	>70 μm	11 mm- 70 mm	<10 MHz, but higher frequency detectors have been used	Suitable for applications such as functional imaging that requires imaging deeper with a larger FOV. This will make it valuable in clinical applications such as neurology and oncology.
Acoustic resolution photoacoustic microscopy (AR-PAM) [41], [53], [55], [57], [69]	>40 μm	3mm- 11 mm	Ranges from 2 MHz to 40 MHz, depending on whether a higher resolution or deeper penetration depth is desired	Generally used to image thicker samples such as lymph nodes, internal organs and larger blood vessels.
Optical resolution photoacoustic microscopy (OR-PAM) [35], [41], [52], [61]–[64]	<10 μm	1–2 mm	Usually >20 MHz for better axial resolution	Useful for imaging smaller samples that are near the surface including the blood vessels, and cells

Chapter 3

Detection mechanism for Photoacoustic Imaging

Two major components for PAI are the photoacoustic signal generator and the detector. The generator is usually the pulse laser which is used to irradiate the sample. Pulse lasers are normally preferred as pulse excitations to produce a better signal to noise ratio (SNR) than continuous-wave excitations [38]. Some excitation capabilities of the pulse laser that dictate the spatial characteristic and contrast include the pulse width and wavelength of the laser [70], [71]. The detector, on the other hand, assumes the role of receiving the acoustic signal that was generated by the illuminated sample. The development of novel detection mechanisms provides additional routes toward improving image quality by offering higher sensitivity, resolution, and SNR.

Several detection mechanisms exist for PAI and each of these detection methods brings about its unique advantages as well as some shortcomings. The detection mechanism used for PAI can be categorized into contact and non-contact-based detection. The physical detectors used in contact-based detection include but not limited to Fabry-Perot Interferometers (FPIs), Micro Ring Resonators (MRRs), piezoelectric transducers and Capacitive Micromachined Ultrasound Transducers (CMUTs). Interferometric method and photoacoustic remote sensing (PARS) are some of the techniques that are currently being explored for non-contact-based detection. More details and explanations about these detection methods will be discussed in the following subsection.

3.1 Contact-based Detection Technique

The four key parameters of the detector, which can affect the image quality are the center frequency, bandwidth, sensitivity, and size [72]. In photoacoustic imaging, the detector's center frequency and bandwidth are two of the most important parameters that determine the image resolution. To attain images with micrometers resolution, a detector needs to have a center frequency and bandwidth that is in the MHz range. Another factor to consider when it comes to choosing a detector is sensitivity. A common measure to determine sensitivity is the noise-equivalent-pressure (NEP). NEP is generally defined as the amplitude of the detected pressure with respect to the noise level. A detector that can pick up a signal in the Pa or sub-Pa range is usually needed to detect photoacoustic signals resulting

from low excitation laser fluences or deeper penetration depths in turbid media such as biological tissues [72]. In designing a PAI system, especially for applications such as minimally invasive surgery (MIS) endoscopes, size is a critical component. Catheters, frequently used for MIS applications, highlight size constraints. Catheters are long tubes with diameters of about 0.5–3 mm hence, a rule of thumb for detectors used for MIS application is that they should have the ability to operate at these device scales [73]. In this chapter, the four more commonly used sensors, FPIs, MRRs, piezoelectric transducers and CMUTs are studied.

3.1.1 Fabry-Perot Interferometer

FPI is a type of interferometer that is made up of a thin transparent film sandwiched between two reflectors [74]. The pressure changes created by the incoming ultrasonic wave causes variation in the thickness and elasto-optic of the structure, which in turn, causes an optical phase shift [74]. An interferometer then transforms this optical phase shift into measurable intensity modulation [75]. The working principle of FPI is illustrated in figure 3.1 (a). FPI has been used as a detector for countless PAI applications [76]–[79]. Hajireza et al. [77] imaged a chorioallantoic membrane (CAM) of a 5-day chicken embryo model in reflection mode with a glancing angle-deposition (GLAD) nanostructured FPI. The resolution and SNR attained with this 18 MHz bandwidth GLAD nanostructured FPI were 7 μm and 35 dB respectively. This is the first reported reflection mode imaging done using FPI *in-vivo* and the experimental set-up is shown in figure 3.1 (b). Ansari et al. [78] designed a forward-looking photoacoustic endoscopy with an FPI array. Fabry–Perot films were deposited on the distal end of each of the 50,000 12- μm fiber core in an image guide bundle which were then placed into a 3.2-mm diameter 76-mm long probe. The acoustic sensor was found to have a 3-dB bandwidth of 34 MHz. 3D imaging of the different phantoms such as synthetic hair, leaf, duck embryo, and mouse skin was demonstrated. In the duck embryo, *ex vivo* imaging of microvasculature was done at a depth of 1 mm and vessels with diameters as small as 50 μm were observed. Vessels with diameters ranging from 53–180 μm were captured 2 mm deep inside the mouse skin.

As FPI sensitivity is not significantly affected by the element size, it can be made using smaller elements so much so that it can be approximated as a point detector, producing sharper images [80]. Since Fabry–Perot sensors can be optically transparent to the excitation beam, they can be used for both

transmission and reflection mode imaging applications [1]. Other advantages of FPI that contribute to the high-resolution images include being more sensitive and less susceptible to electrical noises [81]. That said, one major downside of FPI is the need to do mechanical raster scanning as typically only one FPI element is used for imaging. This means that longer imaging time is required for data collection [80]. In the above photoacoustic endoscopy experiment by Ansari et al. [78], it took about 25 min to form the image. The longer imaging time is due to the need for optical wavelength tuning at every interrogated location.

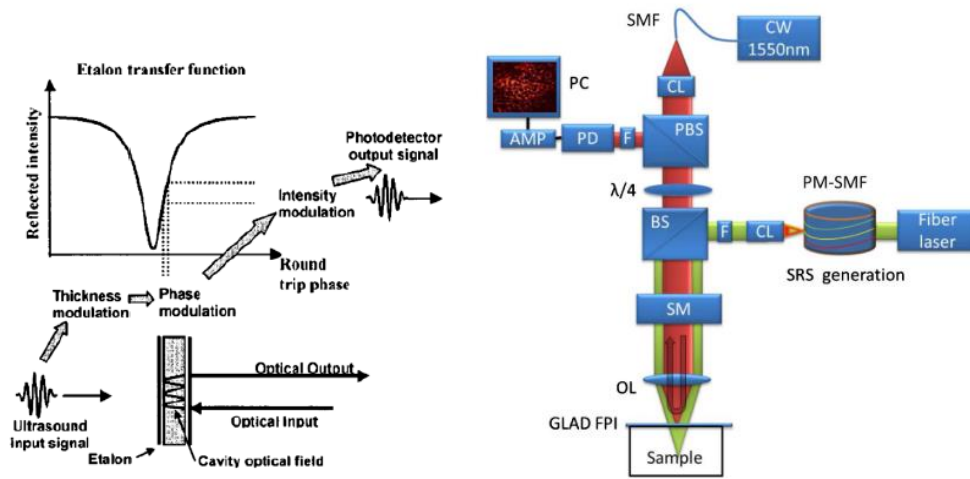


Figure 3.1 The working principle of FPI [2]. (b) Experimental set-up of OR-PAM imaging with GLAD nanostructured FPI [77].

3.1.2 Micro Ring Resonator

MRR comprises of a straight waveguide coupled closely together with a ring waveguide, shown in figure 3.2 (a). The straight waveguide acts as the input and output port of the detector, while the ring waveguide acts as the resonator [3]. Like FPI, the incoming acoustic wave causes a change in the dimension and elasto-optic modulation of the ring waveguide, which in turn alters the refractive index of the MRR [4]. The deviation in the optical path length due to the change in the refractive index induces a shift in the resonance frequency [5]. This shift in resonance frequency is detected by the photodiode, which gives a voltage output that is proportional to this shift in the resonance frequency of the acoustic wave. Li et.al. [4] have fabricated and characterized a transparent MRR used for PAM application. This 250 μm thick MRR with a wide bandwidth of 140 MHz was reported to be highly sensitive and has a

NEP of 6.8 Pa. An axial resolution of 5.3 μm was obtained when imaging a carbon black thin film. The experimental set-up is shown in figure 3.2 (b).

Unlike FPI, the thickness of the film affects the detector's bandwidth instead of its sensitivity [59]. The sensitivity is, nonetheless, dependent on the size of the element. The small element size used in MRR makes wide angular response possible [59]. In fact, in some reports, MRR is found to have better sensitivity than FPI [59]. Since the element size is also related to bending loss, there is a restriction in the reduction of element size as this can impair the FOV [75].

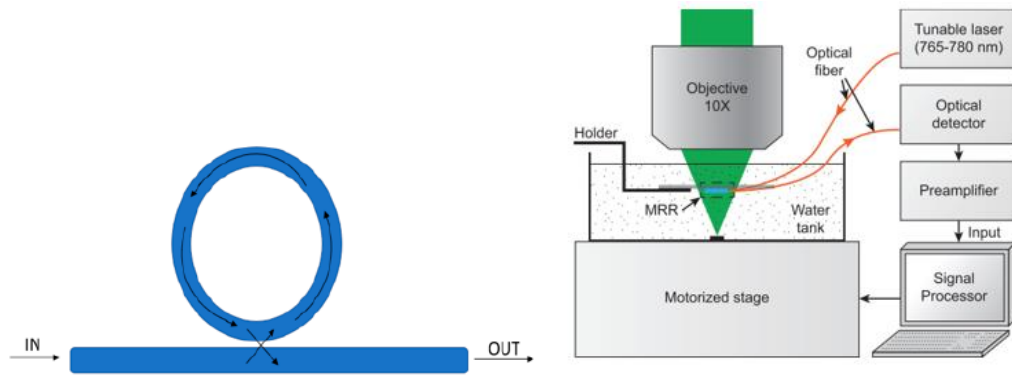


Figure 3.2 (a) Schematic diagram of a micro ring resonator. (b) Experimental set-up of PAM with transparent MRR used in [4].

3.1.3 Piezoelectric Transducer

The piezoelectric effect is the conversion of kinetic energy due to mechanical stress to electrical energy, and vice versa. For years, piezoelectric transducers have been used for numerous purposes going from “sonar,” used in World War 2 to detect submarines [82] to modern day applications such as non-destructive testing [83], energy harvester [84], [85], and biomedical imaging [6], [86]–[88]. Even though piezoelectric and photoacoustic effects were discovered in the 1800s, it was only in the early 1990s when more work was done to explore the photoacoustic effect that reignited researchers’ interest in using PAI for biomedical applications [89]. Since then, various researches were done in this domain. Throughout the years, more research has been done on the piezoelectric transducer to improve its performance. One area that researchers are investigating is the type of piezoelectric materials used for transducer. Various piezoelectric materials are being developed for transducers used in PAI

applications including lead zirconate titanate (PZT) [90], [91], polyvinylidene fluoride (PVDF) [92] and lead magnesium niobate-lead titanate (PMN-PT) [93]. Both PZT and PVDF based piezoelectric transducers have been commonly used for PAI applications [59]. PVDF has the advantage of lower acoustic impedance, while PZT offers a higher piezoelectric coupling coefficient. In this thesis, the piezoelectric transducers discussed are based on the conventional PZT piezoelectric transducers. OR-PAM imaging was first reported by Maslov et al. [94] in 2008. The system was able to achieve a lateral resolution of 5 μm with a penetration depth of more than 0.7 mm. A schematic of the OR-PAM system is shown in figure 3.3. Imaging of microvasculature in the nude was performed with a 75 MHz ultrasonic transducer. This experiment showed the potential of PAI for imaging of blood vessels and achieving micron size resolution.

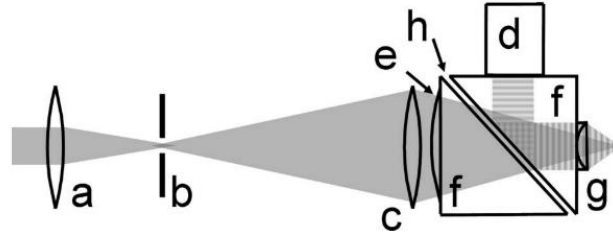


Figure 3.3 Schematic of the OR-PAM system. a: Condenser lens; b: pinhole; c: microscope objective; d: ultrasonic transducer; e: correcting lens; f: isosceles prism; g: acoustic lens; h: silicon oil [94].

Above 1 MHz, piezoelectric transducers have a higher sensitivity and lower thermal noise as compared to the other optical detection methods [32]. Nonetheless, piezoelectric transducers have a limited frequency range. To make a high-frequency array, the transducer elements need to be placed close together to avoid aliasing. The pitch required for a 25 MHz transducer to avoid aliasing is approximately 30 μm [95]. As piezoelectric transducers are typically fabricated using mechanical dicing, it is difficult to keep the elements tightly packed to pitches less than 40 μm [73], [95]. Nevertheless, some groups have managed to alter the conventional manufacturing process and fabricated high-frequency piezoelectric transducer arrays [96], [97]. That said, the inherent properties of the piezoelectric transducer like the small bandwidth is still a constraint in producing high-resolution images. The need for an acoustic matching layer makes piezoelectric transducer bulkier [6]. Besides, piezoelectric transducers also face a huge problem in PAI as it is opaque, which can make delivering of light to the tissue a challenging task [80].

3.1.4 Capacitive Micromachined Ultrasound Transducer

CMUTs, as its name suggests, are micro-electro-mechanical devices fabricated with micromachining, that can be used to receive and transmit ultrasound signals [98]. A typical CMUT cell consists of a membrane suspended over a vacuum gap. A thin layer of metal on top of the membrane forms the top electrode while the silicon substrate forms the bottom electrode [99]. An insulator is stacked on the silicon substrate in order to prevent the top and bottom electrodes from touching. In transmission mode, DC and AC voltages are applied to the electrodes. The DC voltage brings the top and bottom electrodes closer while the AC voltage actuates the membrane to produce an ultrasound signal. During the receiving mode, only DC voltage is applied. The incoming sound wave modulates the gap height based on the wave frequency [100]. As a result, the capacitance of the membrane changes, thereby producing an output current. This output current is converted to a voltage signal and intensified by a transimpedance amplifier. Figure 3.4 (a) shows the set-up of a CMUT in transmission mode while Figure 3.4 (b) shows the CMUT in receiving mode. For PAI applications, CMUTs are mainly used as receivers. Therefore, they can be designed with the sole consideration of optimizing the receiving parameters.

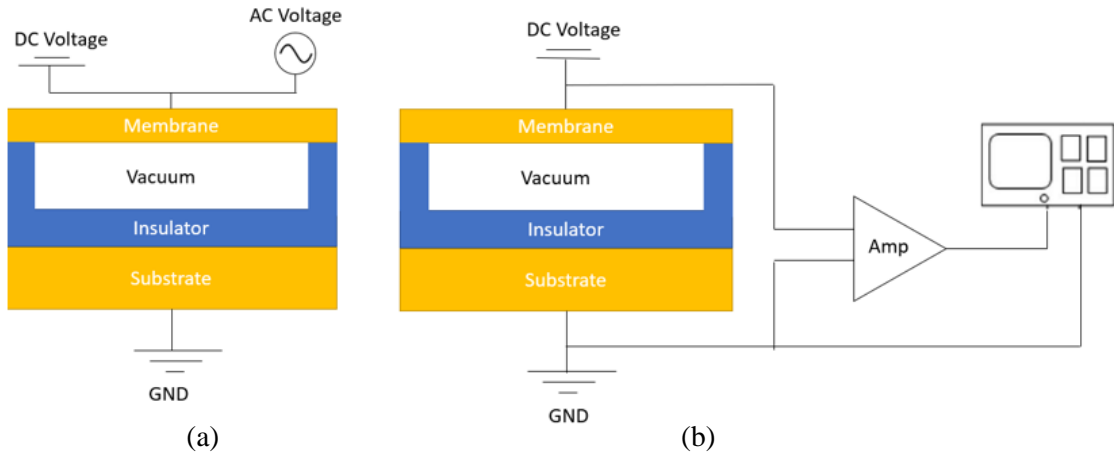


Figure 3.4 (a) Capacitive micromachined ultrasound transducers (CMUT) transmission mode; (b) CMUT receiving mode.

The first reported CMUTs were presented by a research group at Stanford in 1994 with the goal of making an airborne ultrasound transducer that can operate in the MHz range [101], [102]. The motivation to further develop CMUT for other applications resulted from an immersion test where it has shown that CMUTs can provide a larger bandwidth over traditional piezoelectric transducers [101].

Since then CMUTs have been used in a variety of domains ranging from high-intensity focused ultrasound [103], [104], ultrasound imaging [98], [105]–[109], sensing application [110], [111] to non-destructive testing [112]. The use of CMUTs for PAI has been researched for over a decade in mainly two types of applications, the table top application with PACT and photoacoustic endoscopy. Various innovative ideas are being explored for PACT in areas such as 2D array [9]–[12], transparency [13]–[15], and multi-frequency [16]–[18]. In photoacoustic endoscopy, the designs being studied can be split into two different array configurations, phased [19], [20] and ring arrays [21], [22].

A. Photoacoustic Computed Tomography with Capacitive Micromachined Ultrasound Transducer

Two-dimensional Capacitive Micromachined Ultrasound Transducer

An element of CMUT is made of numerous CMUT cells and multiple CMUT elements are used to form an array. A one-dimensional (1D) CMUT array is made of a row of CMUT elements. It uses electronic scanning for the rows and raster scanning for the columns or vice versa to form the image. With a 2D CMUT array, data can be acquired at a faster rate as both the rows and columns are imaged using electronic scanning. In 2005, Wygant et al. [9] were one of the first groups to have started investigating the use of CMUT array for PAI. A 5 MHz 2D 16×16 CMUT array was used to image polyethylene tubes filled with black ink and placed in a $2 \times 2 \times 3$ cm block made of tissue-mimicking material. Both PAI and ultrasound imaging were used to image the phantom. PAI produced a better signal that requires lesser averaging to improve the SNR. This positive outcome opened the door to a new area of research for PAI. Vaithilingam et al. [10] went further by imaging a fishing line and chicken breast phantoms with the 2D 16×16 CMUT array. The fishing line phantom comprised of three 150 μm diameter transparent lines placed alternately between two 180 μm diameter black fishing lines. The chicken breast phantom was constructed with four polyethylene tubes that have an inner diameter of 1.19 mm positioned in chicken breast and covered with agar. The tubes were filled with four different solutions; deionized water, indocyanine green (ICG) solution in deionized water, pig blood, and ICG mixed with pig blood. Data were collected using ultrasound imaging and PAI on both phantoms. Ultrasound imaging was able to detect all the fishing lines and tubes in both phantoms, while with PAI, only the two black fishing lines and three tubes excluding the one containing deionized water in the chicken phantom were captured. The images taken from the ultrasound imaging and PAI is shown in

figure 3.5 (a-d) The axial and lateral resolution acquired using PAI in the chicken phantom at 1.8 cm depth from the CMUT array were 300 μm and 648 μm , respectively.

Kothapalli et al. [11] pushed the limit of the penetration depth for PAI using CMUT array further to 5 cm. Horse hair embedded 2.2 cm, 3.1 cm, 4.1 cm, and 5.3 cm deep inside a chicken breast was imaged using a 5.5 MHz 2D 16×16 CMUT array. Because of scattering, the SNR decreased from 36 dB at 2.2 cm to 23 dB at 5.3 cm deep in the chicken breast. The calculated lateral resolution and axial resolution at 5.3 cm were approximately 720 μm and 370 μm , respectively. The group went on to investigate the sensitivity by varying the concentration of ICG positioned 5 cm deep in the tissue. The SNR showed a decreasing trend as the concentration decreased. The highest SNR of 37 dB was achieved from 10 μM of ICG while the lowest SNR of 13 dB was obtained from 100 nM of ICG.

Other than the design of CMUT, one important area to study is the addressing of large 2D CMUT array. A $N \times N$ CMUT array usually requires $N \times N$ number of connections to produce the image. This can create complications in the wiring of electrical circuits. To reduce the complexity of the electronics required for volumetric imaging, Chee et al. [12] introduced the top orthogonal to the bottom electrode (TOBE) architecture. TOBE involves biasing a column of the CMUT array and transmitting the signal along a row therefore, only N laser pulses and N channels are needed for imaging. Figure 3.5 (e) illustrates the working principle of TOBE. A 3.7 MHz 2D 40×40 CMUT array was used to image three strands of hair placed 2 mm apart in the oil. The calculated lateral and axial resolutions were 866 μm and 296 μm , respectively. This area of research to reduce the complexity of the electronic circuit is essential for CMUT array in real-time PAI.

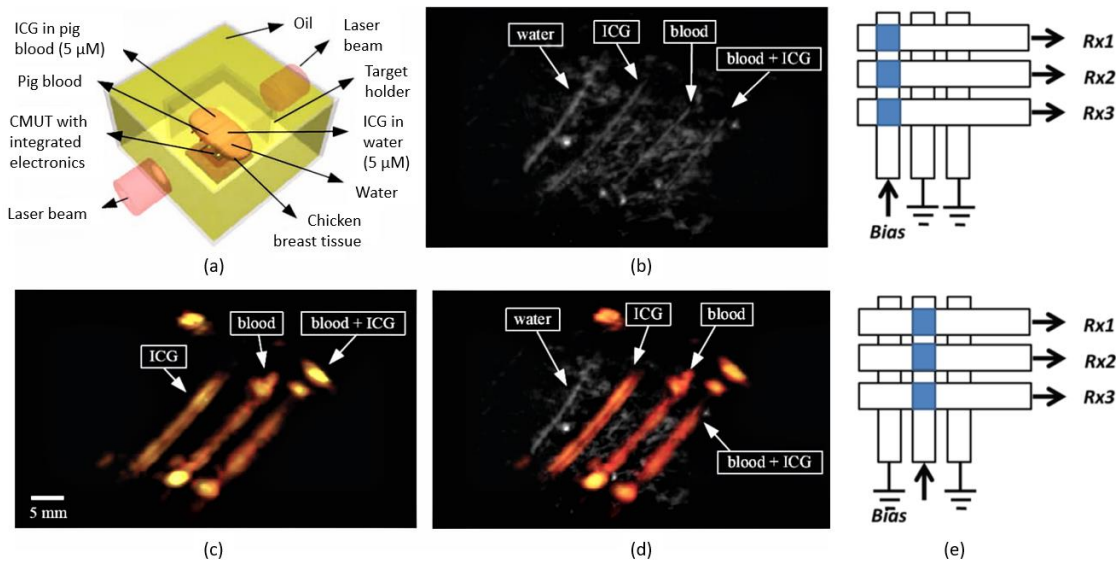


Figure 3.5 (a) Model of the chicken breast phantom, (b) ultrasonic imaging, (c) PAI, and (d) a combination of photoacoustic and ultrasonic imaging [10]; (e) working principle of top orthogonal to bottom electrode TOBE) [12].

Transparent Capacitive Micromachined Ultrasound Transducer

There are two modes of transmission for PAI, forward and backward mode, which are also known as transmission and reflection mode. In clinical applications like endoscopy, backward mode transmission is a more practical approach. Moreover, it helps to eliminate blind spots. One of the challenges that PAI faces is the placement of the laser and the transducer to optimize the illumination of the sample. To address this issue, researchers are coming up with ways to create a transparent CMUT.

Chen et al. [13] designed a photoacoustic imager with a light source cascaded behind an infrared-transparent CMUT. The advantage of this design is that the realignment of the light source and the CMUT is not necessary. The device was used to image a metal wire phantom at varying distances from 2.3–4.5 cm. The measured light transmission of the 1.06 μm laser was about 12%. Zhang et al. [14] improved the transmission efficiency by fabricating a 1.4 MHz CMUT with a glass substrate and ITO bottom electrode, as shown in figure 3.6 (b). The transmittance attained with this device was 30–70% at a wavelength of 700–900 nm. Two phantoms were used for PAI. The first phantom was a 0.7 mm diameter pencil lead immersed 1.5 cm deep in oil. In order to better mimic biological tissue, the second

phantom used was made with a 2.3 mm inner diameter polyethylene tube filled with 50 μM ICG solution suspended in agar gel. In this work, the group mentioned that one of the reasons for low transmission in the visible light range is due to the use of silicon plate, which is not transparent in the visible light range as can be seen in figure 3.6 (a). Li et al. [15] improved the transmission up to 82% in the visible light range by omitting the use of silicon in the fabrication process. The 2 MHz CMUT was characterized and found to have a noise equivalent sensitivity of 95 Pa when biased at 100 V.

Multi-Frequency Capacitive Micromachined Ultrasound Transducer

Another research topic being explored for PAI is the multi-frequency CMUT array. A high-frequency transducer produces images with higher resolution and finer details while a low-frequency transducer experiences lesser attenuation and therefore produces images with higher SNR at deeper penetration depth [113]. With the huge frequency content produced by the tissue from the laser illumination, a multi-frequency CMUT array, where elements of different frequencies are arranged, can be used to capture both the outline and the fine details of the structure at varying depths.

Chee et al. [16] proposed an interlaced multi-frequency CMUT array for PAI as shown in figure 3.6 (d). The lateral resolution obtained from imaging a strand of hair in oil immersion is 673 μm for the 1.74 MHz CMUT and 492 μm for the 5.04 MHz CMUT. The team went on to image a large target like methylene blue and a smaller target such as a strain of hair to analyze the effect of high and low frequency for spectroscopic PAI. The high-frequency element showed a higher SNR when imaging a small hair target, and the low-frequency element had a higher SNR imaging large methylene blue target. In the same year, Zhang et al. [17] fabricated a multiband CMUT array with a radius of 15 μm for the low-frequency component at 3.7 MHz and 10 μm for the high-frequency component at 9.7 MHz. The multiband CMUT array is shown in figure 3.6 (e). In vivo imaging of a zebrafish was done using this device, and a commercial ultrasound transducer. The outline structure of the zebrafish can be identified using the low-frequency transducer and the details of the zebrafish such as the swim bladder, the stripes, and mesenchymal tissues can be seen using the high-frequency CMUT element. This is reportedly the first in vivo PAI done using CMUTs.

Pun et al. [18] further developed the concept by incorporating five different frequencies of CMUTs 2.9 MHz, 3.7 MHz, 5.2 MHz, 7.0 MHz, and 9.3 MHz on a device, as shown in figure 3.6 (f). The transducer

was used to image the head of a mouse where increasing frequency showed an increase in SNR which also results in a more detailed image of the brain of the mouse being captured as seen in figure 3.6 (c). At 2.9 MHz, only the transverse sinus, superior sagittal sinus, and inferior cerebral vein were evident while at 9.3 MHz, on top of those blood vasculatures, superior cerebral vein and olfactory lobe can be seen.

The above experiments present different arrangements of the high and low-frequency elements for a multi-frequency CMUT array. Because of the complexity of the circuit and potential problems that might arise from the cross talk, imaging was done using raster scanning of only one CMUT element at a time. Indeed, a multi-frequency transducer is able to give us more information ranging from minute details to the overall structure of the image. However, to fulfill this, future work would need to address possible problems associated with the complexity of the circuit and cross talk.

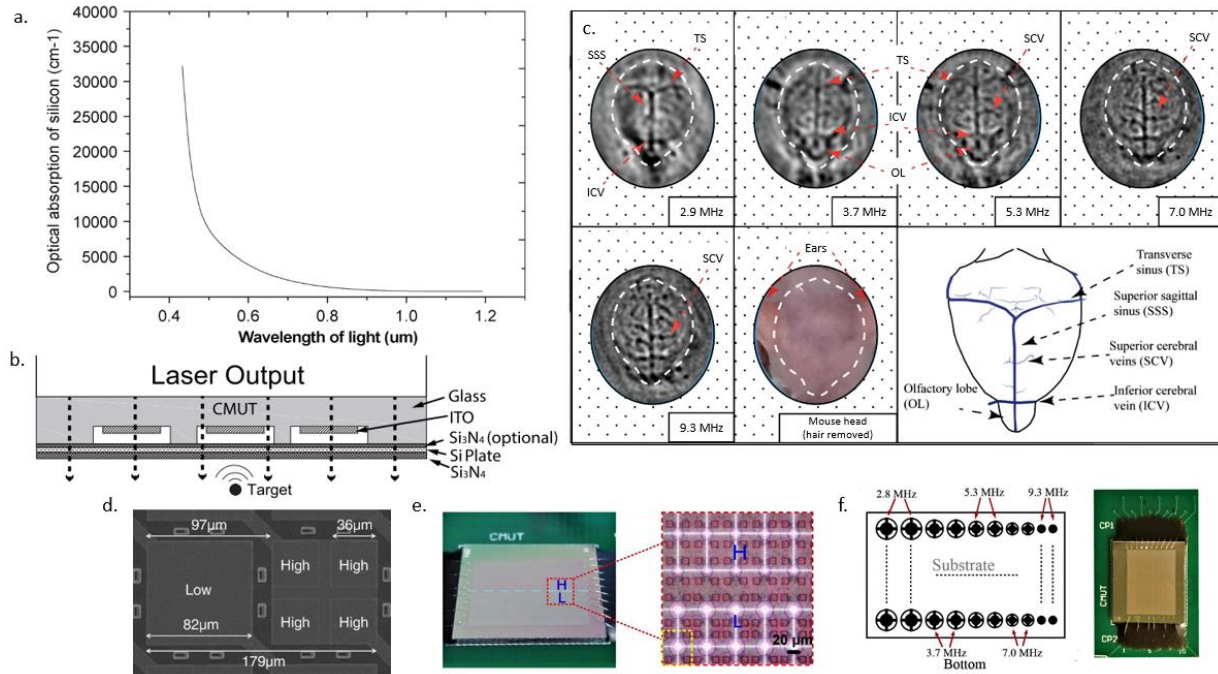


Figure 3.6 (a) Optical absorption of silicon under different wavelength and (b) structure of optically transparent CMUT, (c) imaging of mouse brain using the different frequencies of the CMUT, (d) interlaced CMUT, (e) multi-band CMUT, (f) monolithic multiband CMUT with five frequencies.

B. Photoacoustic Endoscopy with Capacitive Micromachined Ultrasound Transducer

One major limitation of PAI is the restriction in penetration depth because of optical scattering. As CMUT elements can be tightly packed to form the array, CMUT arrays are sufficiently small enough to be easily attached to catheters or endoscope. This brings the detector closer to the tissues, reducing scattering and increasing the resolution. Photoacoustic endoscopy is a change from the larger table top approaches and can be implemented with any of the three imaging modalities, PACT, OR-PAM, and AR-PAM in the two CMUT array configurations, phased and ring array.

Phased Array Capacitive Micromachined Ultrasound Transducer

Phased and ring arrays are two popular configurations for photoacoustic endoscopy using CMUTs. Phased arrays are generally less complicated to design and fabricate as compared to ring arrays. Some research groups had come up with innovative designs for photoacoustic endoscopes using a phased array. Chen et al. [19] designed a needle-shaped CMUT phased array which can be used for MIS applications, shown in figure 3.7 (c). The needle-shaped design is made of 5 MHz CMUT elements with a diameter of 46 μm and is placed on a 2.8–5 mm by 8–18 mm silicon bar. PAI of a lobster nerve cord was done with one element on a rotating stage to collect data at multiple points. Since this design uses a CMUT that is transparent in the near-infrared region, there is minimal shadowing issue. This design showed the miniaturization capability of CMUTs, which is an important factor for MIS endoscopy applications.

Conventionally, CMUTs have been used mainly for ultrasound imaging. The previous work is done by Vaithilingam et al. [20] also showed the limitation of PAI, where it is unable to image transparent objects. Since both PAI and ultrasound imaging have different advantages, Nikoozadeh et al. [20] experimented using CMUT phased array for endoscopic imaging by integrating both PAI and ultrasound imaging into a catheter. The structure of the catheter is shown in figure 3.7 (b). The 6.64 MHz CMUT array is able to image the outline of the tumor that is 15 mm deep in a phantom model of a mouse's subcutaneous kidney.

Ring Array Capacitive Micromachined Ultrasound Transducer

The circular view provided by a ring array gives a wider field of view and reduces the occurrence of reconstruction artifacts [21]. Moreover, a ring array design can make use of the empty spaces around

the probe to optimize the space available. Vaithilingam et al. [21] designed one of the first CMUT ring array for PAI, an inward-looking cylindrical transducer array in 2006 as shown in figure 3.7 (a). A 3 MHz CMUT ring array was used to image an ink-filled polyethylene tube placed in a tissue-mimicking material. The axial and lateral resolution attained from the experiment was 350 μm and 4 mm. On top of the advantages of a circular view, as stated above, this inward-looking cylindrical transducer array also has the advantage of enclosing the target. This immensely helps to minimize the formation of motion artifacts and increase the image resolution.

Nikoozadeh et al. [22] proposed another interesting design where four CMUT ring arrays with different diameters and center frequencies are stacked together in a probe. A structure of this CMUT ring array is illustrated in figure 3.7 (d). The frequencies of the rings are 16 MHz, 12 MHz, 8 MHz, and 6.5 MHz. In this paper, only 8 MHz and 6.5 MHz CMUT ring arrays were used to image a 13 mm spring and a custom wire phantom with ten 0.15 mm diameter nylon fishing lines. Both rings were able to produce images of the metal spring at 45 mm deep and the custom wire phantom at 15 mm deep. This design made use of the advantages of both multi-frequency and ring arrays to produce a photoacoustic endoscopy probe.

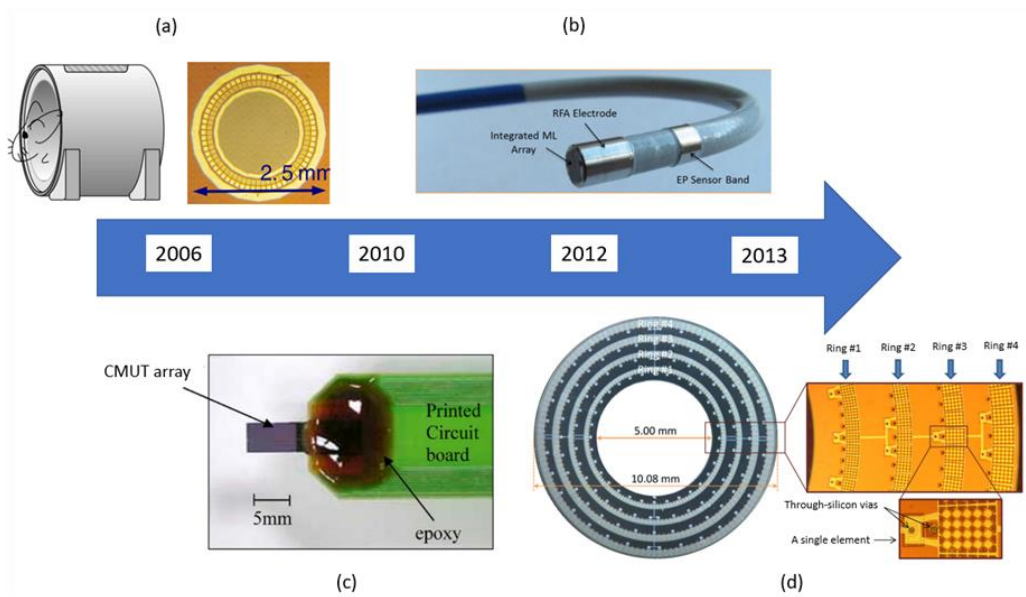


Figure 3.7 Timeline of CMUT designs for PAI endoscopes [76]–[79]; (a) inward-looking cylindrical transducer, (b) 9F MicroLinear CMUT ICE catheter; (c) miniature needle-shaped CMUT (d) integrated ring CMUT array.

3.1.5 Discussion of the Physical Sensors

Leveraging on their property of high sensitivity over a large bandwidth, FPIs and MRRs can produce images with higher resolution than piezoelectric transducers and CMUTs . On the downside, the penetration depth of FPI and MRR is limited to millimeters. Moreover, because of their delicate fabrication, it is difficult to fabricate FPI and MRR arrays. Some issues with using only a single sensor element for imaging are the reduction in imaging speed as observed in the above experiments and the inevitable formation of motion artifacts. One solution to these issues is to fabricate these sensor elements into an array [114]. The fabrication of FPI array is not as straight forward as fabricating piezoelectric transducer and CMUT arrays, additional steps are needed. After fabricating the FPI elements, these individual elements are placed onto a substrate or fiber one at a time to form the array. Careful calibration is required before the FPI array can be used for real-time imaging. For MRR, fabricating it into an array can be a challenging task as they rely on the optical coupling. On the contrary, piezoelectric transducer and CMUTs can be made into an array and uses electronic scanning to produce the image [80], [95]. Hence, piezoelectric transducer array does not face the issues that FPI and MRR encounter with mechanical raster scanning which makes it a more suitable candidate for real-time imaging. Table 2 shows the sensitivity, advantages and disadvantages of the different detectors.

Table 2 The performance of different acoustic detectors along with their advantages and disadvantages in PAI applications.

Detectors	Sensitivity	Advantages	Disadvantages
Fabry–Perot interferometer (FPI) [76]–[79], [115], [116]	NEP: 80–300 Pa	- High-resolution image with small active area	- Challenging to fabricate into an array - Mechanical scanning - Smaller penetration depth
Micro-ring resonator (MRR) [4], [5], [117]	NEP: 35–105 Pa	- Wide angular response - Low NEP over a wide frequency range	- Challenging to fabricate into an array - Mechanical scanning - Smaller penetration depth
Piezoelectric transducer (PZT) [90], [118], [119]	SNR: 18–22 dB	- Most matured and readily available - Deeper penetration depth	- Opaque - Not CMOS compatible - Difficulty in fabricating high-density array
Capacitive micromachined ultrasound transducer (CMUT) [9]–[22], [120]	SNR: 22–87 dB	- CMOS compatible - High-density arrays can be fabricated - Deeper penetration depth	- DC voltage is needed - Dielectric charging

3.2 Non-contact-based Detection Technique

In most photoacoustic imaging technique, coupling media such as water or oil will be needed to connect the sample and the detector. This will help to reduce the attenuation that arises due to the acoustic impedance mismatch between the sample and air. However, the need for coupling media will make it difficult for PAI to be used in *in-vivo* clinical applications where touching the delicate tissues will cause contamination and damage. Thus, non-contact-based detection methods would help to resolve this issue.

3.2.1 Interferometry

Interferometric detection methods have been around for several decades with the earliest interferometers, Michelson interferometers (MI) and Mach-Zender interferometers (MZI) used for detection of particle displacement in the 1960s [72]. Besides the excitation laser used to illuminate the sample, another interrogation laser will be needed for detection. The interrogation laser beam is split into two optical paths, one of the laser paths will head towards the sample to measure the perturbation while the other will form the reference arm. Both beams will be recombined and measured at the output where the summation of their electric field gives the amplitude and phase shift that resulted from the photoacoustic effect. The interference signal obtained will be indicative of the ultrasonic amplitude generated. There are a few interferometric set-ups that have investigated for photoacoustic imaging including heterodyne interferometer [121], homodyne interferometer [122] and two-wave mixing interferometer [123]. Heterodyne interferometer makes use of two close frequencies optical waves to generate a new wave with its intensity proportional to the product of the amplitudes of the two input signals. Tian et.al. [121] imaged an *ex-vivo* swine brain model with a Mach-Zehnder configuration of the heterodyne interferometer (RSV-150, Polytec) operating at 1550 nm. The beam was split into two paths, the measurement and the reference beams. The measurement beam was focused onto the sample and the backscattered light was redirected into the interferometer and then the photodiode. The reference beam experiences a steady frequency shift induced by the Bragg cell before heading into the same photodiode. This set-up was able to achieve a spatial resolution of 1.1 mm for the *ex-vivo* swine brain model completely non-contact. However, this was attained at the expense of complex synchronization and processing algorithms. Moreover, the accuracy is determined by several parameters including laser wavelength instability, photodetector nonlinearity, and electronic processing noise. Hochreiner et al. [123] have presented a non-contact PAI using an optical fiber-based Mach-

Zehnder interferometer along with optical amplification. An optical parametric oscillator (OPO, Continuum Surelite OPO Plus) was pumping at 532 nm to excite the sample while a 1550 nm laser was used to detect the generated photoacoustic signal. An aiming laser at 635 nm was coupled into the detector head to simplify the adjustment of the detection beam. The change in the relative phase between the reference arm and the sample was measured at the photodiode and the image was reconstructed with a Fourier domain reconstruction algorithm. Three-dimensional imaging of a tissue-mimicking phantom, a silicon tube filled with ink immersed in a milk/water emulsion and a polymer surface, and two-dimensional imaging of chicken skin were demonstrated. Figure 3.8 illustrates the schematic of the experimental set-up. In this experiment, ultrasound gel was applied onto the muscle tissue to attain the two-dimensional image. Thus, this would mean that this imaging set-up is not entirely non-contact. Moreover, this method requires a complex set-up and processing algorithm for imaging.

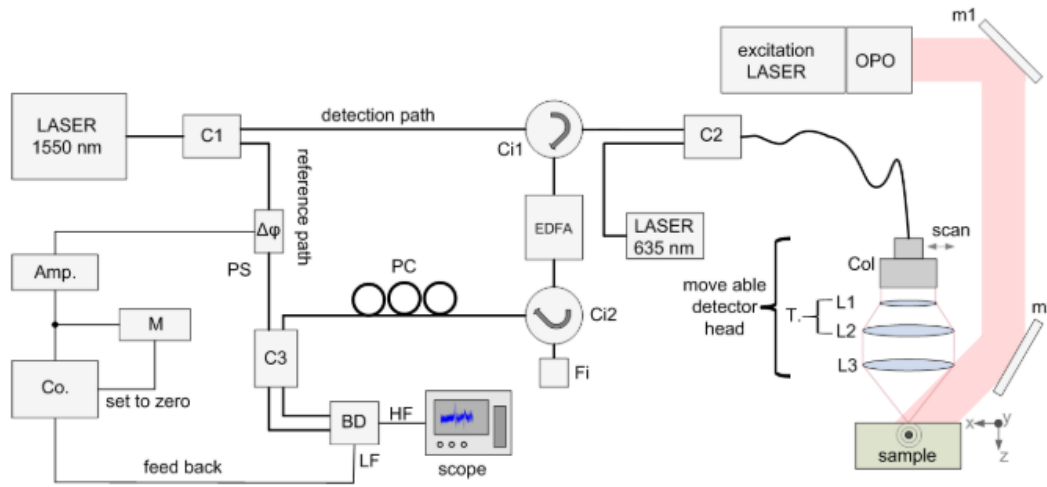


Figure 3.8 Schematic of the experimental set-up [123].

Numerous interferometric imaging methods have demonstrated a certain level of non-contact for PAI application, but this usually comes with a more complicated set-up or processing method. Moreover, interferometric detection methods usually detect the surface oscillation from the induced pressure wave to form the image. Due to the highly sensitive nature of this method, other factors such as external vibration, surface and subsurface oscillation, can cause unwanted interference.

3.2.2 Photoacoustic Remote Sensing

In 2017, Hajireza et al. [7] introduced a new method of detection that only focuses on the intensity of reflectivity changes. Photoacoustic Remote Sensing (PARS) is able to sense the pressure generated at the subsurface origin without the need for a resonator and interferometric detection architecture. In PARS, a low-coherence interrogation beam is used to reduce the phase-modulation sensitivity. The interrogation beam is a continuous-wave laser that will be co-focused with a scanned excitation laser onto the sample. The initial pressure rise from the photoacoustic effect first alters the elasto-optics refractive index, which will in turn change the intensity of the back-reflected of the interrogation beam. This change in reflectivity will be proportional to the optical absorption of the excitation pulse. However, the change in reflectivity due to the index modulation is small. It is found that if the time-varying refractive index is close to the refractive boundary, which acts as a refractive index step, the change in reflectivity becomes more significant. An illustration of this concept is shown in figure 3.9.

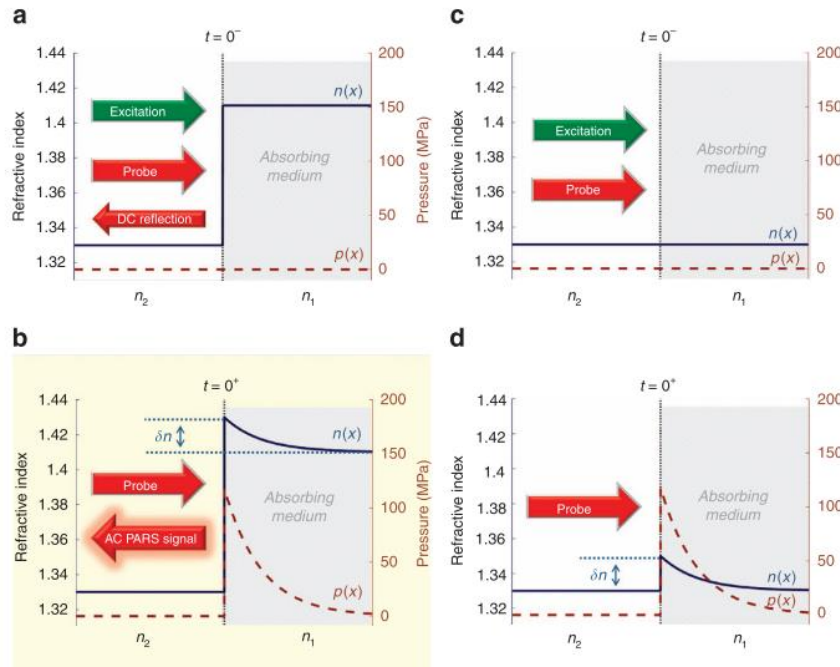


Figure 3.9 Diagram of the PARS mechanism. (a) If a refractive index profile $n(x)$ exists at the boundary of an absorbing media having a refractive index n_1 , a DC reflection of a probe beam is expected before pulsed excitation occurs ($t=0^-$). (b) The excitation beam has been absorbed ($t=0^+$), and thermoelastic excitation of the absorber generates an initial pressure profile $p(x)$. This, in turn, perturbs the existing refractive index by δn , which produces an AC modulation in

the reflected probe beam proportional to the absorption. Note that the DC component is not shown in this figure for simplicity. (c, d) If there is no existing refractive index step, then the small δn modulation generated by the absorption of the excitation beam creates a negligible AC signal variation (not shown) [7].

The PARS detection mechanism has been explored for many uses ranging from in-vivo imaging of mouse ear [7] to microscopic histology of unstained human tissues [8]. Hajireza et al. [7] demonstrated the PARS effect and managed to image the melanoma tumor and surrounding vasculature of the mouse ear. A 532 nm nanosecond-pulsed laser for was used excitation while a 1310 nm a low-coherence laser was employed for interrogation. A diagram of the experimental set-up is presented in figure 3.10. This proposed system was able to image the superficial microvasculature in melanoma tumors as shown in figure 3.11 and attained a lateral resolution of $\sim 2.7 \mu\text{m}$.

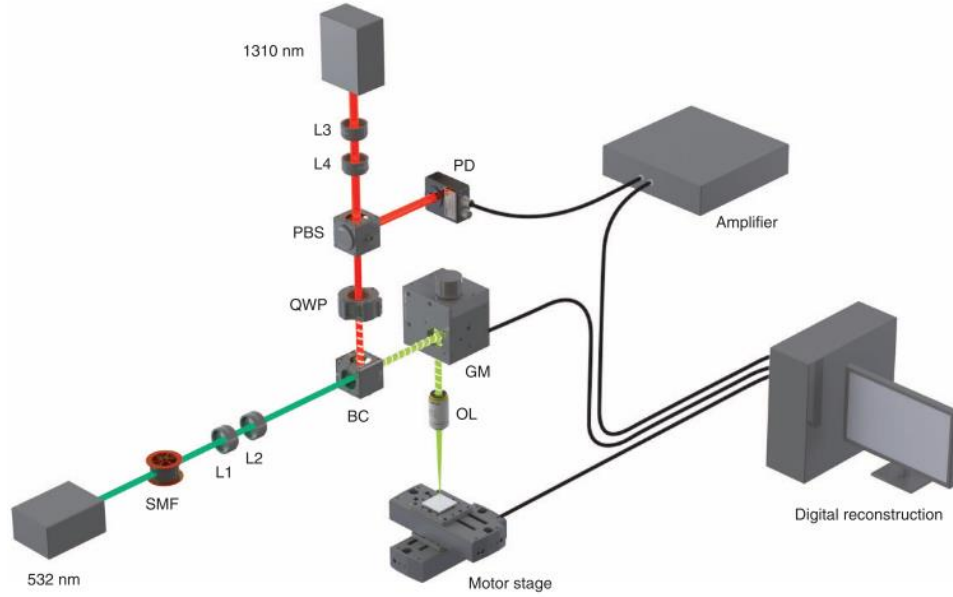


Figure 3.10 Experimental setup. PARS microscopy with 532-nm excitation and 1310-nm integration beams. BC, beam combiner; GM, galvanometer mirror; L, lens; OL, objective lens; PBS, polarized beam splitter; PD, photodiode; QWP, quarter-wave plate; SMF, single-mode fiber

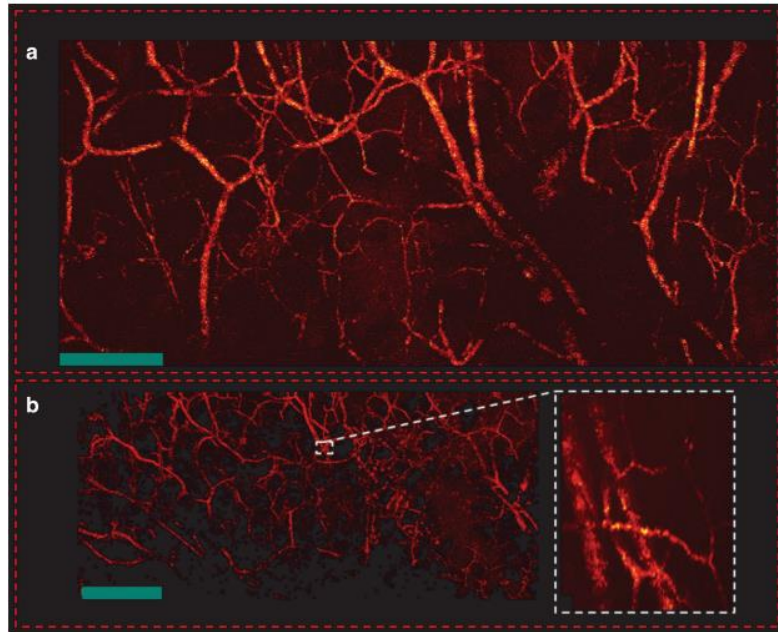


Figure 3.11 In vivo en-face mouse ear images. (a) PARS images using two-axis lateral mechanical scanning. (b) Larger field of view images using mechanical scanning as well as a zoomed in image of both capillary beds and larger blood vessels using fast scanning mirror

The PARS system has a simpler imaging system as compared to the interferometry detection method and is also able to achieve complete non-contact detection. Without phase sensitivity, the PARS system can eliminate the noise that is generated by the surrounding environment. However, the time-resolved signals used for PARS imaging do not contain the time-of-flight information therefore, the depth-resolved information is lost. Bell et al. [124] have managed to address this problem by making use of the difference between pulsed-interrogation optical coherence tomography scan-lines with and without excitation pulses to provide coherence-gated depth-resolved PARS imaging. This concept has been validated with simulation however, experimental results were not presented.

3.3 Summary

Photoacoustic detection mechanisms have been extensively studied for years. Depending on its application, different detection mechanisms have their unique advantages and disadvantages. The contact-based detection method offers a variety of physical detectors that can be used in the sensing of photoacoustic signals. In this thesis, the more common physical detectors, their working principle along with their pros and cons are discussed. Non-contact detection techniques have an apparent benefit where they eliminate the need for coupling media which helps to minimize the risk of contamination. This would make them suitable for applications that require a sterile environment. However, the penetration depth of these imaging methods might be less optimal for AR-PAM and PACT applications. In the next chapter, a photoacoustic imaging experiment with a 2.2 MHz piezoelectric transducer and the PARS detection mechanism is demonstrated and studied.

Chapter 4

Optical Resolution Photoacoustic Microscopy Imaging Experiment

4.1 Receive sensitivity of Piezoelectric Transducer

The receive sensitivity of the transducer is an important parameter in the study of physical detectors for OR-PAM applications. In this experiment, a 2.25 MHz unfocused commercial piezoelectric transducer (I3-0204-S-SU, Olympus) was selected to receive the photoacoustic signal. The receive sensitivity of the piezoelectric transducer was characterized with a 2.5 MHz CMUT in vegetable oil. The output pressure of the CMUT was first measured in oil immersion using the hydrophone (HGL-0200, Onda) which was placed about 22 mm away from the CMUT. A 20 V DC bias was applied and a pulser/receiver (NDT 5073PR, Panametrics) was used to drive the CMUT to generate ultrasound pulses. Figure 4.1 shows a schematic of the experimental set-up. With the time domain of the ultrasound signal and the calibration data of the hydrophone provided by the manufacturer (0.322 mV/kPa), the output pressure of the CMUT was obtained. For the receive sensitivity test, the hydrophone was replaced with the piezoelectric transducer while keeping the the same distance. The piezoelectric transducer was connected through the pulser/receiver to the digital oscilloscope. Figure 4.2 and Figure 4.3 display the ultrasound signal received by the piezoelectric transducer and the frequency spectrum respectively. Using the output pressure from the CMUT and the receive signal attained from the digital oscilloscope, the receive sensitivity of the piezoelectric transducers was calculated to be approximately 4.2 mV/kPa.

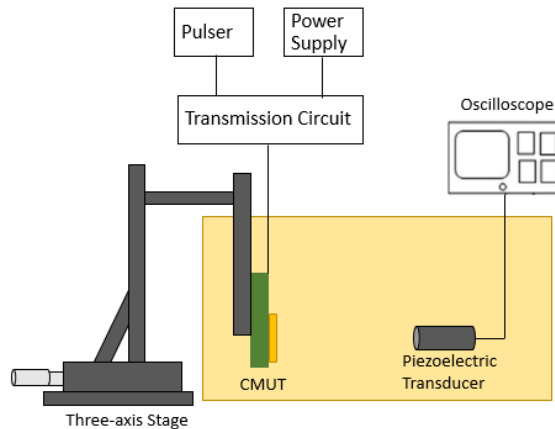


Figure 4.1 A schematic of the experimental set-up for receive sensitivity.

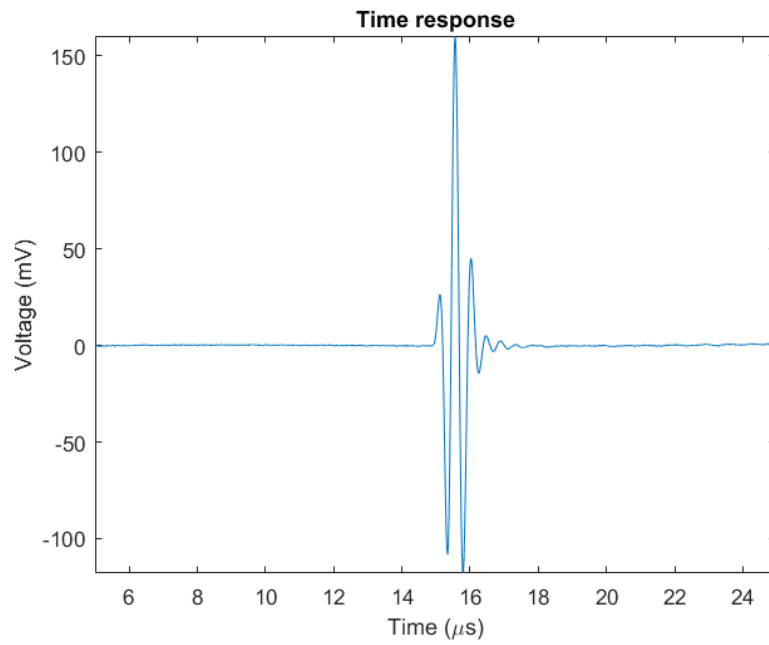


Figure 4.2 Graph of time response of piezoelectric transducer as the receiver.

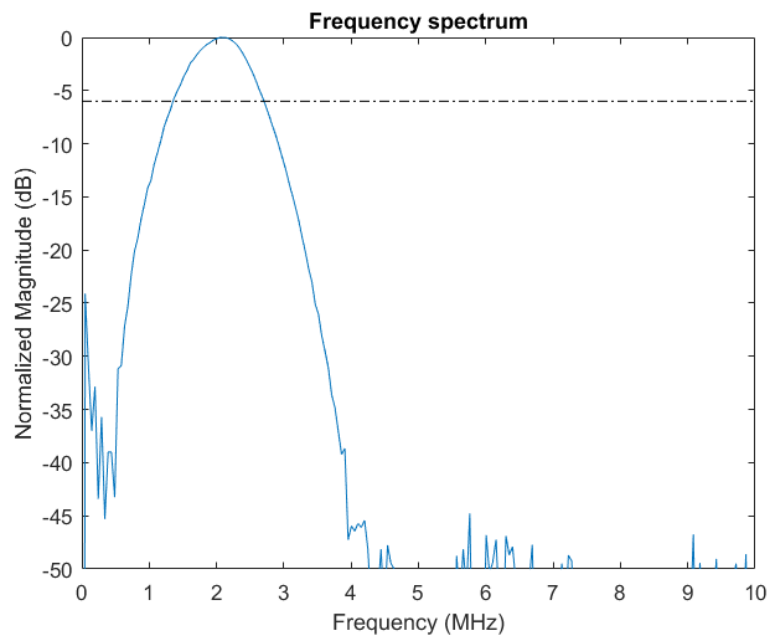


Figure 4.3 Graph of frequency spectrum of piezoelectric transducer as the receiver.

4.2 Photoacoustic Imaging

4.2.1 Experimental Set-Up

The photoacoustic signals can be detected in two modes, transmission and reflection modes. When the excitation laser hits the sample, the photoacoustic signals are generated in different directions. In transmission mode, photoacoustic signals are detected below the sample while reflection mode is the sensing of photoacoustic signals that have bounced off the sample. Figure 4.4 illustrates OR-PAM imaging in reflection and transmission mode. A 532 nm pulsed laser operating at a pulse-repetition rate of 80 kHz, was optically focused to excite the sample. The excitation beam was spatially filtered and collimated to a beam size of approximately 5 mm before it goes through a 0.4 NA objective lens (M Plan Apo NIR 20X, Mitutoyo). The generated photoacoustic signals were then received by the 2.25 MHz piezoelectric transducer in transmission mode. The piezoelectric transducer was connected to the pulser/receiver box (NDT 5073PR, Panametrics) which filters the signal with a bandpass filter of 1 kHz to 20 MHz and amplifies the signal with a gain of 39 dB. A x-y axis galvanometer mirror system (GVS012/M, Thorlabs Inc.) was used to scan the beam. The fast axis of the mirror was set at 89 Hz while the slow axis mirror was running at 2.2 Hz and an image with a FOV of $180 \times 180 \mu\text{m}^2$ was captured. The signals were collected and digitized with a 16-bit digitizer gauge card (CSE161G4, Gage Applied) at a sampling rate of 25 M/s.

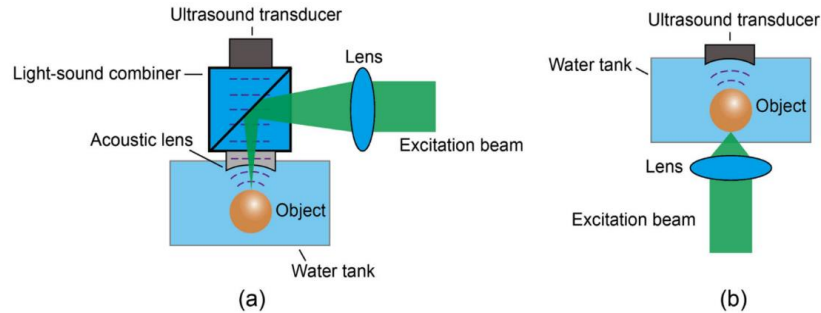


Figure 4.4 (a) Reflection mode (b) Transmission mode [36].

For the PARS system, the detection was set in reflection mode and the piezoelectric transducer was replaced with a 637 nm continuous-wave laser. After passing through the zoom collimator, the collimated interrogation beam was directed to the polarized beam splitter which separates the beam into two paths. The first beam path will be converted from a vertically polarized light to a circularly polarized light after going through the quarter-wave plate. Thereafter, the polarized beam was

combined be with the excitation beam at the dichroic mirror. The second beam path is the reference arm and would head towards the balanced photodiode (PDB425-C, Thorlabs Inc.). The intensity of the reflected beam detected by the balanced photodiode would be an indicator of the amount of pressure wave produced as a result of the photoacoustic effect. Both the excitation and interrogation beams are co-focused with the 0.4 NA objective lens. A schematic of the experimental set-up is shown in figure 4.5. The output of the photodiode was filtered with a high pass filter, 100 kHz and a low pass filter, 22 MHz before being digitized with the 16-bit digitizer gauge card at a sampling rate of 200 M/s for signals collection.

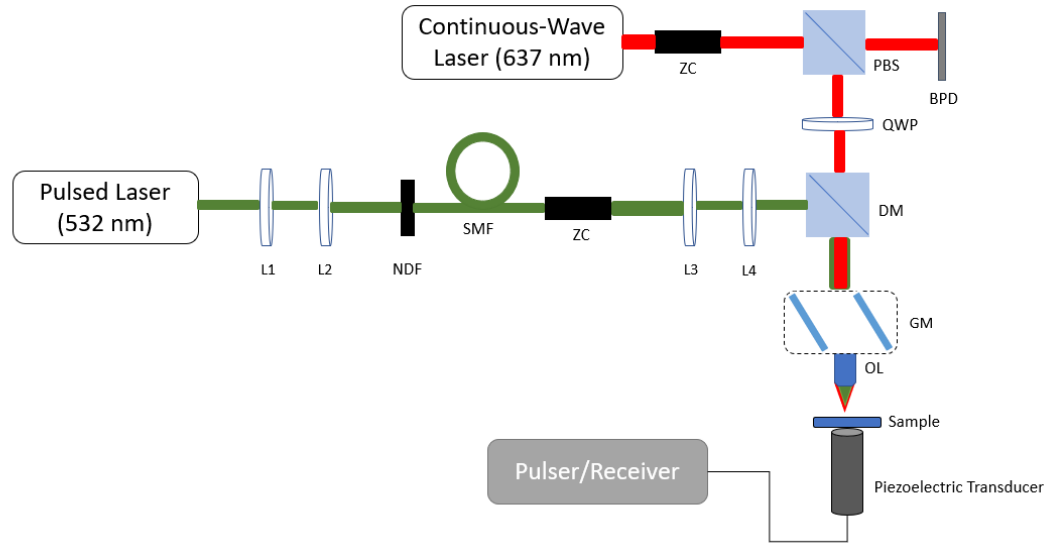


Figure 4.5 Schematic of the experimental set-up of photoacoustic imaging. ZC: Zoom collimator. PBS: Polarized Beam Splitter. BPD: Balanced Photodiode. QWP: Quarter-wave Plate L: Lenses. NDF: Neutral Density Filter. SMF: Single-mode fiber. DM: Dichroic Mirror. GM: Galvanometer Mirror. OL: Objective Lens.

4.2.2 Result

Images of $\sim 7 \mu\text{m}$ carbon fiber were attained with both the conventional piezoelectric transducer in transmission mode and the PARS system in reflection mode as shown in figure 4.4 (a) and (b) respectively. These images were formed using the maximum amplitude projection method and the positional data taken from the scanning mirror. The pulse energy of the excitation beam used for both detection mechanisms was $\sim 1.8 \text{ nJ}$ while 0.4 mW integration power was used for the interrogation PARS system.

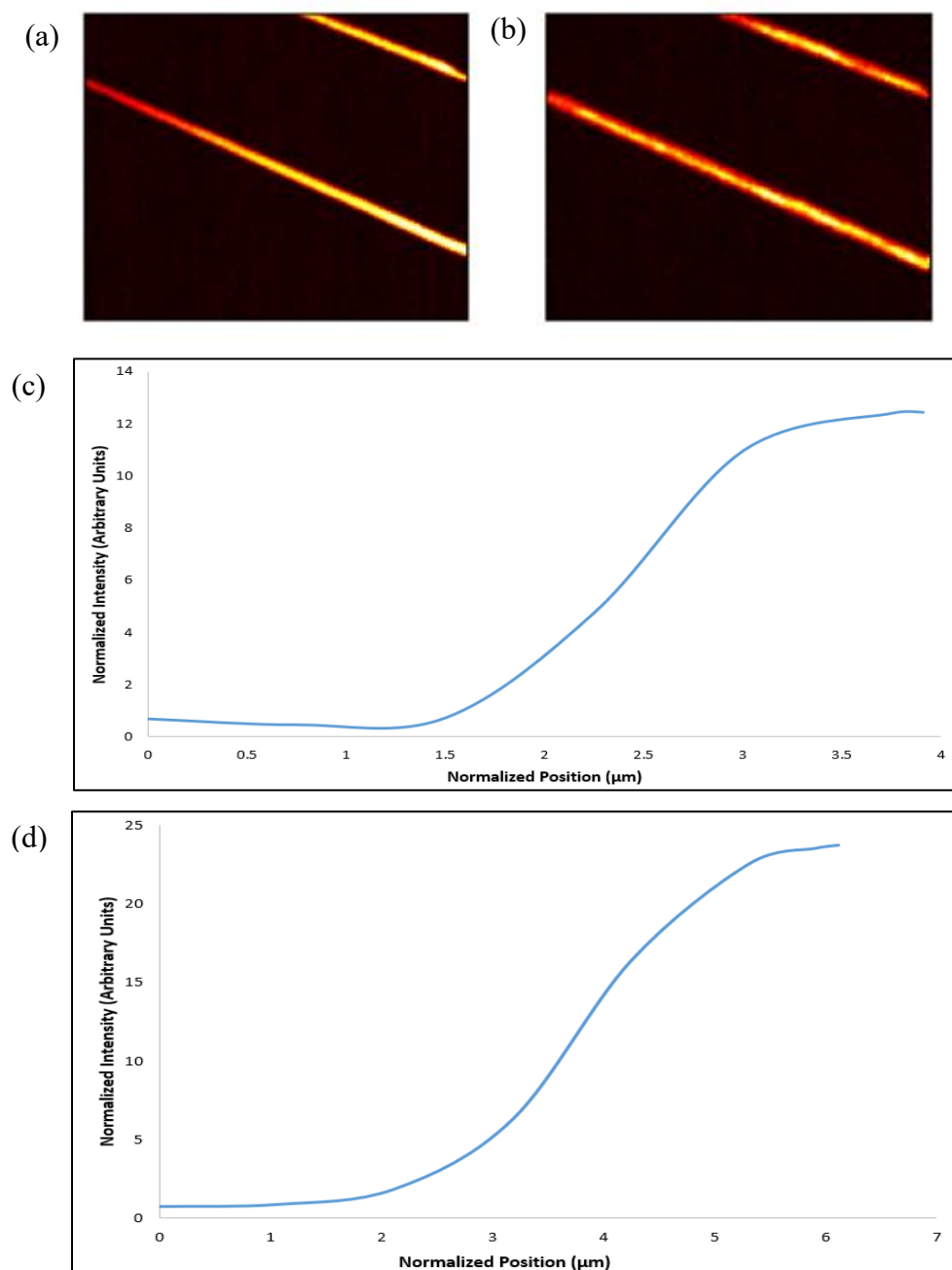


Figure 4.6 B scans of carbon fiber imaged with (a) piezoelectric transducer and the (b) PARS system. Graph of the normalized intensity against the normalized position of the carbon fiber imaged using (c) the piezoelectric transducer and (d) the PARS system.

The lateral resolution was characterized using a B-scan image of the carbon fiber obtained with both the piezoelectric transducer and the PARS system. With the resolution being defined as the width from 10% to 90% of the normalized intensity, the lateral resolution with the piezoelectric transducer and the PARS system had a lateral resolution of $\sim 1.5 \pm 0.3 \mu\text{m}$. The graph of the normalized intensity against the normalized position of the carbon fiber imaged using a piezoelectric transducer and the PARS are shown in figure 4.6 (c) and (d). The sensitivity of the system was later studied using the SNR. The SNR is defined as the maximum intensity over the standard deviation of pixel values in empty frames. The SNR of both the photoacoustic detection mechanism was 30 dB with the piezoelectric transducer and 29 dB with the PARS system.

Table 3 Comparison table between the piezoelectric transducer and PARS.

	Piezoelectric Transducer	PARS System
Mode of Detection	Transmission Mode	Reflection Mode
Signal to Noise Ratio	30 dB	29 dB
Lateral Resolution	$\sim 1.5 \pm 0.3 \mu\text{m}$	

4.2.3 Discussion

In this study, a 2.25 MHz piezoelectric transducer and the PARS system were used for OR-PAM imaging of carbon fiber. Both detection methods were characterized against their B-scans of carbon fiber. The piezoelectric transducer and PARS system have a similar SNR and lateral resolution. In this experiment, a 637 nm continuous-wave laser was used in the PARS system for detection. One downside to using a visible wavelength like 632 nm over other wavelengths like 1310 nm is the increase in the amount of light scattering. Besides, there are other possible factors that can be optimized to enhance the performance of the PARS system such as raising the power of the detection mechanism. Overall, both detection mechanisms produce similar results. Therefore, the determining factor to decide which detection method to use would be the application. The piezoelectric system will be advantageous for use in application where penetration depth is a huge concern such as AR-PAM and PACT while the PARS system will be useful in application where the risk to contamination is not be tolerated.

Chapter 5

CMUT Modeling

The benefits of having piezoelectric transducer-based detectors over FPIs and MRRs apply to a CMUTs as well. Additionally, CMUTs have other advantages over piezoelectric transducers. With an acoustic impedance that is similar to tissues, CMUTs do not need a matching layer, making it less bulky. In general, the fractional bandwidth achievable by CMUTs is over 100% while piezoelectric transducers can typically only attain a fractional bandwidth of 60–80% [125]. As previously stated, one of the important parameters for PAI is the receiving sensitivity of the transducer [72]. Zheng et al. [125] compared the receive sensitivity of a 2.63 MHz CMUT and a 2.43 MHz piezoelectric transducer (Olympus). The result showed that the CMUT element had a higher received sensitivity of 22.57 mV/kPa while the piezoelectric transducer only attained a receive sensitivity of 4.28 mV/kPa. Furthermore, with micromachining, CMUTs can be easily made into any geometry and dimension to meet design specifications [126]. On top of that, micromachining is similar to the fabrication technique used for complementary metal-oxide-semiconductor (CMOS). Therefore, CMUTs can be easily integrated with electronics, integrated circuit (IC) which can help to reduce parasitic capacitance in electronics and improve the SNR [95]. The improvement in SNR can be seen from the experimental results attained by Vallet et al. [90]. The group did an experiment to compare the use of the PZT piezoelectric transducer and CMUT probes for PAI. In the experiment, 2.6 MHz (Vermon) and 3.2 MHz (ACULAB,) CMUT probes, and 7.2 MHz (Prosonic Co.) and 7.3 MHz (Esaote S.p.A) piezoelectric transducer probes were used to image agar phantoms. Based on the results attained, the CMUT probes had a larger fractional bandwidth with an SNR of up to 14 dB and contrast to noise ratio (CNR) of up to 20 dB higher than piezoelectric transducers.

In recent years, piezoelectric material has also been used to fabricate micromachined ultrasound transducers. This transducer is known as the piezoelectric micromachined ultrasound transducer (PMUT). The creation of PMUTs addresses some of the problems that traditional piezoelectric transducers faced and shares some of CMUTs' advantages such as being able to integrate with IC and ease of fabricating a high-frequency array. PMUTs have reportedly been used for PAI purposes [127], [128]. In comparison to CMUTs, PMUTs, like its counterpart, the conventional piezoelectric transducers still possess the inherent property of having a smaller bandwidth. In addition to that, there

is a huge challenge in the designing and fabrication of PMUTs as their resonance frequency are very sensitive to the residual stress of the membrane [129]. Thus, fabricated PMUTs usually perform worse than what they can theoretically do. This potentially makes PMUTs a less attractive transducer.

5.1 Working Principle of Capacitive Micromachined Ultrasound Transducers

The performance of CMUTs can be affected by design factors such as the type of material for fabrication, the diameter of the plate and the gap height. Thus, CMUT modeling will help to explain how these design factors can affect the mechanical, electrical and acoustic behavior of CMUTs. This will also allow the tailoring of the different design parameters to suit various applications. In this section, the numerical analysis and the finite element analysis of CMUTs will be explored.

5.1.1 Numerical Analysis

The fundamentals of a CMUT can be studied using the plate theory. Based on Kirchhoff's theory for an axisymmetric plate, the displacement profile of a circular plate CMUT cell clamped on both edges under uniform applied pressure can be derived using the following formula.

$$x(r) = \frac{P_0}{64D}(r^4 - 2r^2r_0^2 + r_0^4) \quad (5.1)$$

where P_0 is the external pressure applied to the plate, r_0 is the radius of the plate and r is the radial position of the plate from the center, $r = 0$ at the center. D is the modulus of rigidity which is defined as:

$$D = \frac{Et_0^3}{12(1 - \nu^2)} \quad (5.2)$$

where t_0 is the thickness of the plate, E and ν is the plate material's Young's modulus and Poisson ratio.

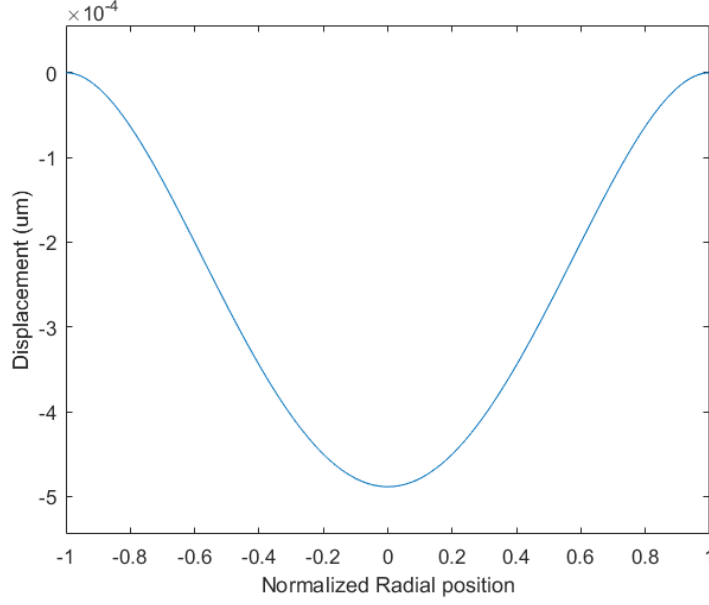


Figure 5.1 Deflection of the CMUT with respect to its radial position when only atmospheric pressure is applied.

From figure 5.1, it can be observed that the peak displacement happens at the center of the plate, where $r = 0$.

$$x_{pk} = \frac{P_0 r_0^4}{64D} \quad (5.3)$$

The displacement of the plate, when averaged over the entire plate, is found to be one-third of the peak displacement, x_{pk} .

$$x_{avg} = \frac{\int_0^{r_0} 2\pi r x(r) dr}{\pi r_0^2} = \frac{P_0 r_0^4}{192D} = \frac{x_{pk}}{3} \quad (5.4)$$

The behavior of CMUTs can be further explored using the lumped mass model. A second-order system, also known as the mass-spring-damper model, is commonly used to obtain the behavioral characteristics of CMUTs. The CMUT cell can be considered as a parallel-plate capacitor where the top moveable plate is separated from the bottom fixed plate by an air gap. As the top plate moves towards the bottom plate, a resistive mechanical force by the spring opposes the electromechanical force. A schematic of the spring-damper model of a CMUT cell is shown in figure 5.2.

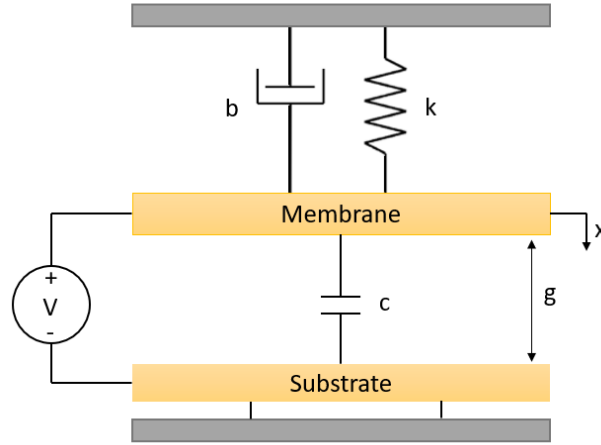


Figure 5.2 Mass spring-damper model of CMUT.

The general equation of CMUT as a mass-spring-damper model can be expressed as:

$$F_{mechanical} + F_{electrostatic} = 0$$

$$m\ddot{x} + b\dot{x} + kx = \frac{-\epsilon_0 A}{2} \left(\frac{V(t)}{g - x} \right)^2 \quad (5.5)$$

where m is the equivalent mass of the plate, b is the damping coefficient, k is the spring constant, g is the gap height and x is the displacement of the plate. ϵ_0 is the permittivity of free space, A is the area of the top plate and $V(t) = V_{dc} + V_{ac}$ is the DC and AC voltage applied and g is the initial gap height. Under the static condition, both acceleration and velocity are zero.

$$\frac{\epsilon_0 A}{2} \left(\frac{V_{dc}}{g - x} \right)^2 = kx \quad (5.6)$$

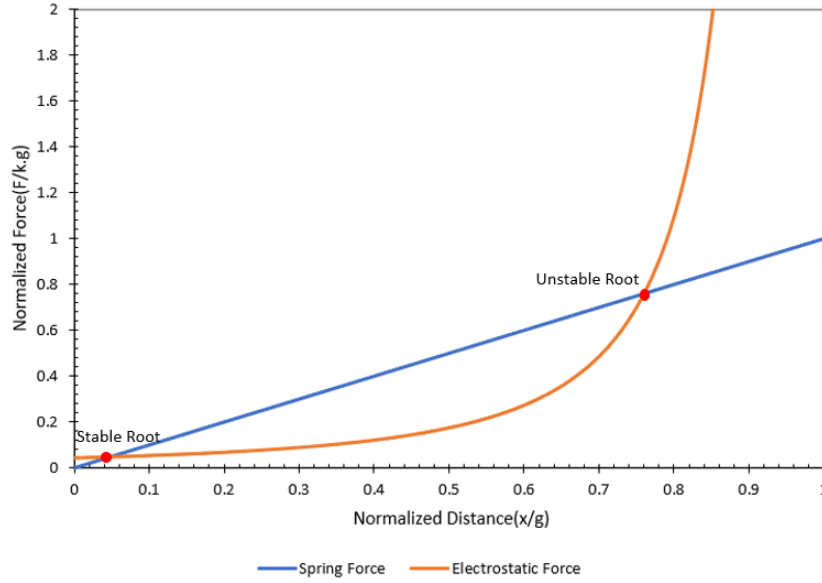


Figure 5.3 The normalized force against the normalized distance of the spring force and electrostatic force.

Thus, with the assumption that the displacement of the plate is generally smaller than the thickness of the plate, the displacement will vary linearly with the applied force under static condition.

$$k_0 = \frac{F}{x} = \frac{P_0 A_0}{x_{avg}} = \frac{192\pi D}{r_0^2} \quad (5.7)$$

Based on the mode shape, the modal mass can be found using the equivalent force produced by the spring constant. The modal mass of the fundamental mode shape where the shape of static deflection is identical to the vibration is found to be as follows.

$$m = \rho_0 t_0 \int_0^{r_0} 2\pi r \frac{x(r)^2}{x_{avg}} dr = \frac{9}{5} \pi r_0^2 \rho_0 t_0 = \frac{9}{5} A_0 \rho_0 t_0 = \frac{9}{5} m_0 \quad (5.8)$$

where ρ_0 , t_0 and m_0 is the density, thickness actual mass of the plate respectively.

In most applications, CMUTs operate in immersion. One major source that contributes to the energy losses when CMUT is operating in immersion is the medium load impedance. The acoustic impedance of the medium can be defined as the ratio of the acoustic pressure in the medium to the associated particle velocity. It is a function of the frequency and can be modeled using the Bessel and Struve

function. For a circular plate piston transducer operating within an infinite rigid baffle, the acoustic impedance is given as:

$$Z_m = Z_0 \left[1 - \frac{J_1 2Kr_0}{Kr_0} + j \frac{H_1 2Kr_0}{Kr_0} \right] \quad (5.9)$$

where $Z_0 = \frac{\rho_{med}}{V_{med}}$ and $K = \frac{2\pi}{\lambda}$

J_1 is the first order of the Bessel function, H_1 is the first order of the Struve function. Z_0 is the plane wave impedance which is calculated based on the ratio between the density of the medium, ρ_{med} over the speed of the sound in the medium, V_{med} . K is the wave number. An estimate for the first order of the acoustic impedance can be found if the operating frequency and the radius of the plate is small relative to the speed of sound, $Kr_0 \ll 1$. The real part of the acoustic impedance, radiation impedance will contribute to the acoustic damping while the imaginary part will add to the mass term thereby causing the resonance frequency to shift [101].

$$Z_m = Z_0 \left[\frac{K^2 r_0^2 + j Kr_0}{1 + K^2 r_0^2} \right] \quad (5.10)$$

$$R_m \approx Z_0 \left[\frac{\pi K^2 r_0^4}{2} \right] \quad (5.11)$$

$$X_m \approx Z_0 \left[\frac{8Kr_0^3}{3} \right] \quad (5.12)$$

A. Pull-in Voltage

One crucial parameter to ensure the safe operation of CMUT is the pull-in voltage. Pull-in voltage is the point where the electrostatic and the mechanical forces are equal, resulting in the top electrode snapping down on the substrate. Hence, it is important to operate CMUTs below the pull-in voltage. In static condition, the pull-in voltage for the CMUT plate occurs at the point where the electrostatic force is equal to the mechanical force, resulting in the plate snapping down to a substrate.

When the gradient of the electrostatic force overcomes the gradient of the mechanical force, the pull-in phenomenon happens. In this case, there will only be one root to the equation. Differentiating both sides by x ,

$$\frac{\varepsilon_0 A}{2} \left(\frac{V}{g-x} \right)^2 = kx$$

$$k_{soft} = \frac{\varepsilon_0 A V^2}{(g-x)^3} \quad (5.13)$$

By plugging equation (5.13) back into equation (5.6),

$$\frac{\varepsilon_0 A}{2} \left(\frac{V_{PI}}{g_{PI}} \right)^2 = k_{soft} x \quad (5.14)$$

$$\frac{\varepsilon_0 A}{2} \left(\frac{V_{PI}}{g_{PI}} \right)^2 = \frac{\varepsilon_0 A V_{PI}^2}{(g_{PI})^3} (g - g_{PI})$$

$$\frac{1}{2} = \frac{1}{(g_{PI})} (g - g_{PI})$$

$$g_{PI} = \frac{2}{3} g \quad (5.15)$$

From equation (5.15), it can be noted that the gap height of where pull-in occurs is $\frac{2}{3}$ of the original gap. Thus, the pull-in voltage can be expressed as $V_{PI} = \sqrt{\frac{8kg^3}{27\varepsilon_0 A}}$.

B. Spring Softening Effect

Based on equation (5.14), it can be observed that an applied bias would change the electrostatic force thereby altering the spring constant. As the applied bias increases, the top electrode moves closer towards the bottom electrode, which also reduces the spring constant. This phenomenon is known as the spring softening effect. The inherent spring constant of the CMUT's membrane would have an added term that would take into account the applied bias. The modified spring constant can be expressed as:

$$k = k_0 - k_{soft} = \frac{192\pi D}{r_0^2} - \frac{\varepsilon_0 A V_{PI}^2}{(g-x)^3} \quad (5.16)$$

Figure 5.3 shows that there are 2 roots, stable and unstable roots, in the solution of the mass-spring-damper model. The result of the spring softening is the increase in displacement of the CMUT cell as shown in figure 5.4.

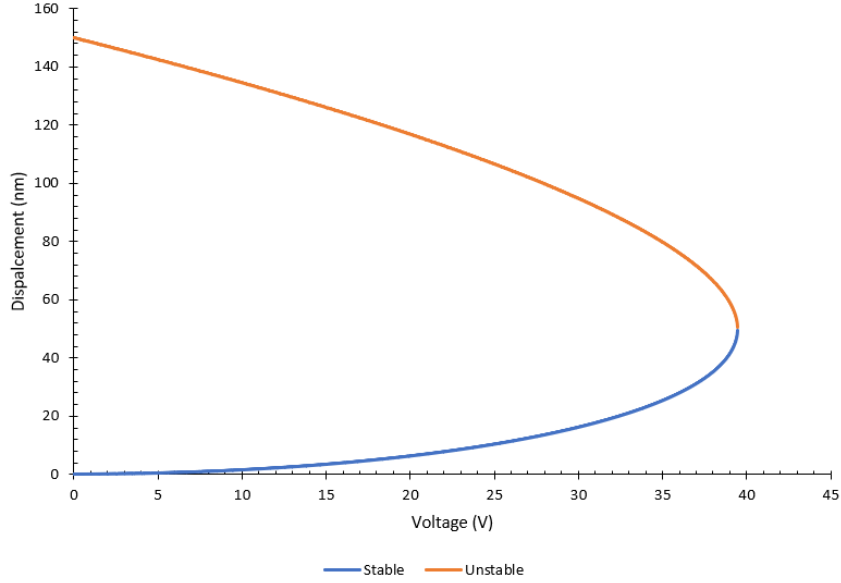


Figure 5.4 Stable and unstable roots of displacement under different bias voltages

C. Resonance Frequency and Fractional Bandwidth

The resolution of the image is largely determined by the resonance frequency and fractional bandwidth of the transducer. Under undamped condition, the first mode frequency also known as the fundamental resonance frequency of a clamped circular plate operating in air can be expressed as:

$$f_0 = \frac{1}{2\pi} \sqrt{\frac{k_0}{m_0}} = \frac{0.47t_0}{r_0^2} \sqrt{\frac{E}{\rho_0(1-v^2)}} \quad (5.17)$$

A wider bandwidth is generally desired as it helps to enhance the imaging resolution. The fractional bandwidth of the transducer is the reciprocal of the quality factor. When the quality factor is greater than 0.5, equation (6.19), is used. However, if the quality factor is less than 0.5, the system is overdamped, and resonance frequency would be considered undefined.

$$FBW = \frac{f_H - f_L}{f_0} = \frac{1}{Q} = \frac{R_m}{\sqrt{k_0 m_0}} \quad (5.18)$$

The above equation, equation (5.17) is used to attain the resonance frequency in the absence of damping. Thus, when CMUTs are operating in immersion, equation (5.19) is used to calculate the resonance frequency instead.

$$f_r = f_0 \sqrt{1 - \frac{Z_m^2}{4k_0 m_0}} = \frac{\frac{0.47t_0}{r_0^2} \sqrt{\frac{E}{\rho_0(1-v^2)}}}{\sqrt{1 + 0.67 \frac{\rho_{med} r_0}{\rho_0 t_0}}} \quad (5.19)$$

D. Small-signal circuit model

The small-signal circuit is another model that can be used to study the frequency response as well as the transmit and receive sensitivity of the CMUT. The mechanical system can be converted into the electrical circuit by replacing the forces with the electrical components. In the modeling of the small-signal circuit, a two-port network made of the electrical and mechanical domains is constructed. Figure 5.5 shows a diagram of CMUT's small-signal circuit.

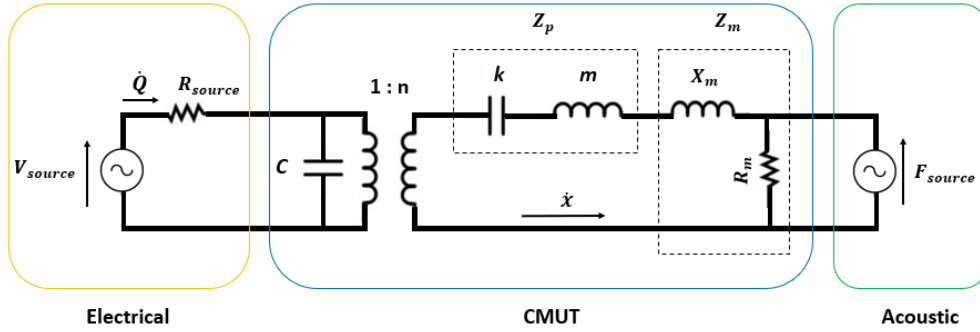


Figure 5.5 CMUT's small-signal circuit model Z_p is the plate impedance which comprise of the equivalent spring constant, k and the mass, m . Z_m is the medium impedance which consists of the resistance, R_m and the reactance, X_m . In transit mode, $F_{source} = 0$ while in receive mode, $V_{source} = 0$.

$$\dot{Q} = \frac{\partial(CV)}{\partial t} = \frac{\varepsilon_0 AV}{(g-x)^2} = CE \dot{x} \quad (5.20)$$

where $C = \frac{\varepsilon_0 A}{g-x}$, $E = \frac{V}{g-x}$

The electromechanical transformer ratio, n can be derived using the ratio between the input current and the output velocity.

$$n = \frac{\dot{Q}}{\dot{x}} = \frac{\varepsilon_0 AV}{(g-x)^2} = CE \quad (5.21)$$

E. Receive Sensitivity

Receive sensitivity is an essential parameter to consider in the study of photoacoustic imaging where CMUT is only used to detect the photoacoustic signal. In the receive mode, photoacoustic pressure hits the plate thereby changing the capacitance which produces the output current. From the circuit model, it can be noted that the maximum receive sensitivity occurs at the resonance frequency, when the impedance of the inductor and capacitor cancels each other out.

$$\dot{Q} = \frac{\varepsilon_0 AV}{(g - x)^2} \dot{x} = CE \dot{x} = CE \frac{PA}{Z_m} \quad (5.22)$$

$$S_{RX} = \frac{\dot{Q}}{P} = \frac{CEA}{Z_m} = \frac{nA}{Z_m} \quad (5.23)$$

where P is the input pressure. Based on equation (6.24), it can be deduced that a smaller gap height and a larger surface would increase the receive sensitivity of the CMUT.

5.1.2 Finite Element Analysis

The finite element method is a numerical method used to solve partial differential equations in engineering and mathematical models. COMSOL Multiphysics is one of the finite element modeling tools available in the market. Despite being more time-consuming, COMSOL modeling is able to provide a more accurate method that can be used to better understand the static and dynamic performance of CMUTs in air and immersion. Table 4 shows the parameters used in this model. The axisymmetric 2D CMUT cell constructed in this model consists of the insulator, vacuum cavity, inner and outer membrane of the CMUT cell. A schematic of the model is shown in figure 5.6. Electromechanics was selected and applied to the solid domains and the cavity. Linear Dielectric was assigned to the solid domains for the calculation of structural mechanics. Other than the membrane, all the solid domains are set as fixed constraints. This will allow the membrane to vibrate freely. The bottom surface of the inner membrane was excited by the terminal of the top electrode while the top layer of the insulator is grounded.

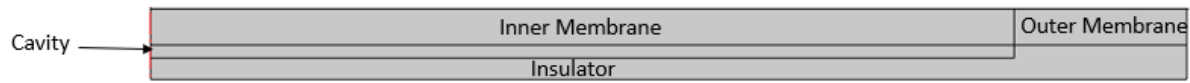


Figure 5.6 2D model of CMUT used in COMSOL

Table 4 Parameters used in modeling

	Material	Thickness	Diameter
Membrane	Silicon	500 nm	25 μm
Cavity	Air	150 nm	25 μm
Insulator	Silicon Dioxide	350 nm	30 μm

The resonance frequency can be found by doing a frequency sweep. At resonance frequency, the displacement of the membrane will be at its maximum. With an applied bias voltage of 30V, the displacement of the CMUT cell in-air and in-immersion under frequency sweep is shown in figure 5.7 and figure 5.8. From figure 5.7 and figure 5.8, it can be observed that CMUT operating in-immersion has a lower resonance frequency, smaller displacement and wider bandwidth which can be attributed to higher damping,

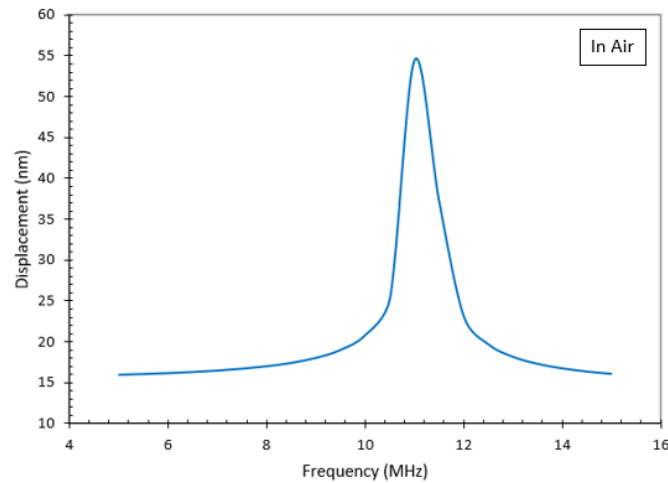


Figure 5.7 Frequency spectrum of CMUT operating in air under a bias voltage of 30V

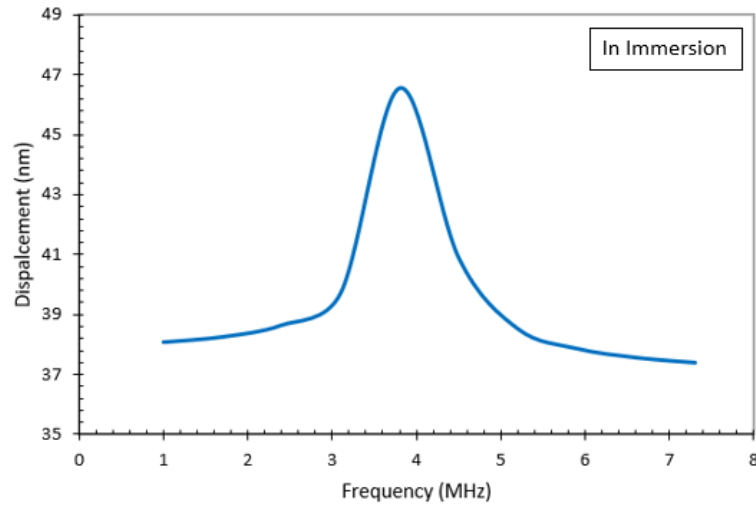


Figure 5.8 Frequency spectrum of CMUT operating in immersion under a bias voltage of 30V

The displacement of the membrane relative to different bias voltage is examined using the numerical and finite element analysis. Both methods show similar results in the displacement of the CMUT membrane under different bias voltage as shown in figure 5.9. A slight difference between both methods is expected as the finite element analysis is a multi-degree of freedom model and therefore able to provide a more accurate result.

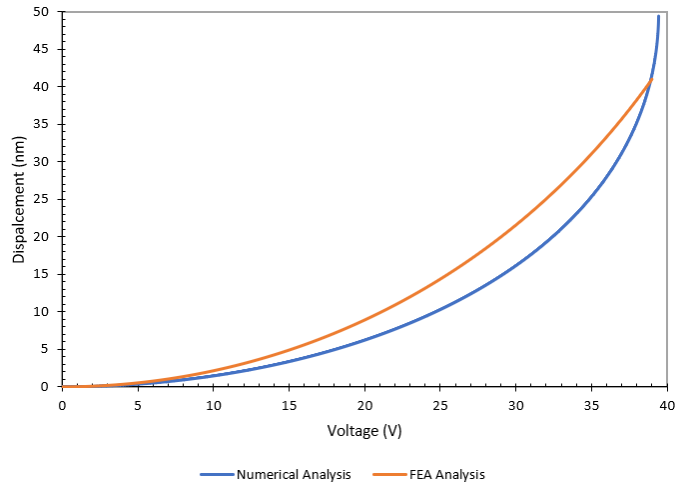


Figure 5.9 Displacement of CMUT membrane under different bias voltage using numerical and finite element analysis

5.2 Fabrication

The advantage of CMUTs which allows it to be miniaturized with enhanced performance lies in the fabrication process. There are generally two main methods for the fabrication of CMUTs namely surface micromachining and wafer bonding. The key difference between both methods lies in the way the cavity is made.

5.2.1 Surface Micromachining

Traditional surface micromachining was adopted for the fabrication of CMUTs since the start of the production of CMUTs in 1994. In this method, the structure is formed layer by layer from the bottom to the top. Figure 5.10 illustrates a general process flow of fabrication of CMUTs using surface micromachining. A sacrificial layer, which is usually made of polysilicon, is deposited between the top membrane and the insulator. Release holes will be patterned using photolithography, and wet etched to remove the sacrificial material. The cavities will be formed by sealing the release hole with chemical vapor deposition under low pressure. However, the need to pattern release holes causes downsides such as the decrease in fill factor which will in turn result in low output power and sensitivity. The problem with the decreased fill factor will be more prominent in the fabrication of high-frequency CMUT where the cell diameter is already small. Other problems that arise include limited control over thickness uniformity and gap height.

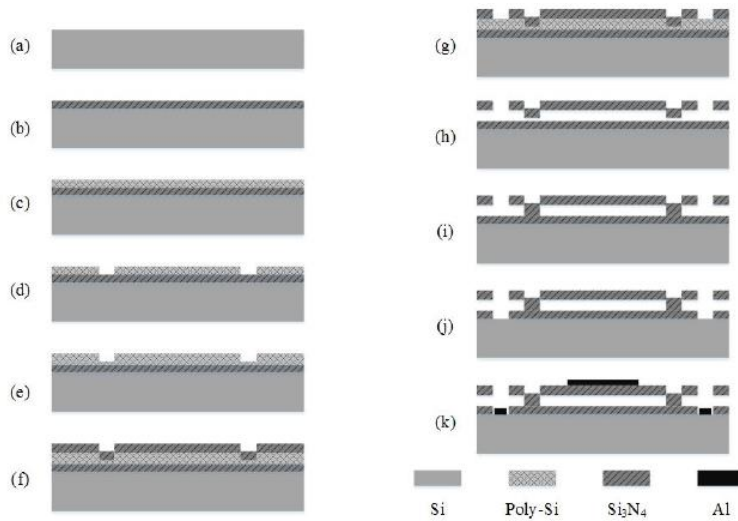


Figure 5.10 Process flow of fabricating CMUTs with surface micromachining [130]

5.2.2 Wafer Bonding

The second fabrication method is the wafer bonding technique. Wafer bonding as its name suggests is the binding of the top and bottom wafers. The bottom wafer, usually a highly doped silicon wafer is first patterned using photolithography and etched with oxide reactive-ion etching to form the cavity. Under high force and vacuum condition of the wafer bonder, the top wafer, which is also the membrane, and the bottom wafer will be brought together to form a bond. A high temperature annealing process is needed thereafter to strengthen this molecular bond. Figure 5.11 illustrates the process flow of fabricating CMUT with wafer bonding method. This method is more cost-efficient requiring only 4 masks as compared to the surface micromachining that requires 6 masks process [131]. Wafer bonding technique allows the mechanical properties of the fabricated CMUTs to be more predictable and controllable. Furthermore, with this method since etch holes are not needed. This will increase the active area thereby increasing the sensitivity. With this method, vacuum sealing is much easier and there is better control over the gap height [131].

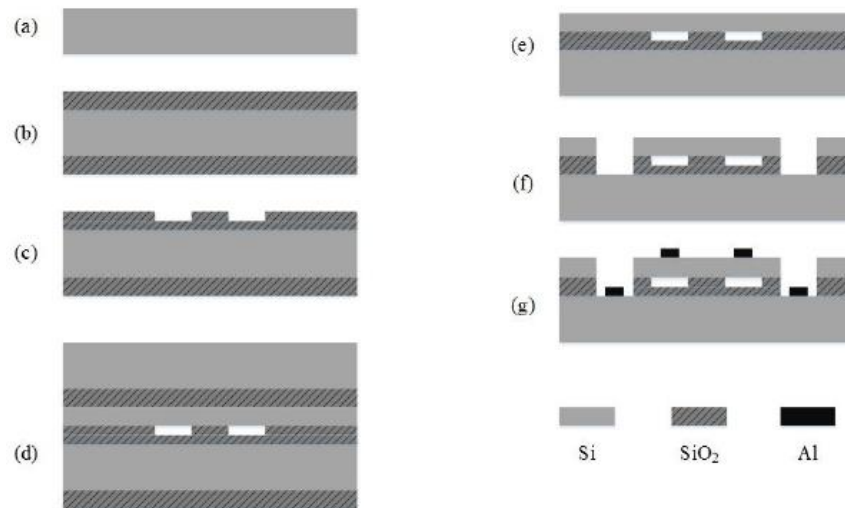


Figure 5.11 Process flow of fabricating CMUTs with wafer bonding [130]

In most cases, Silicon-On-Insulator (SOI) wafers are used as the membrane for direct wafer bonding process. Despite being readily available, there are some disadvantages. Firstly, with limited wafer thickness, there will be constraints in the CMUTs' design. Moreover, it is difficult to purchase sub-micron thick SOI wafers [111]. Thus, our group has developed a new process that uses silicon nitride

as the membrane. By using silicon nitride instead of SOI wafers, the thickness of the device can be customizable. Additionally, the number of photomasks needed can be reduced from four to three thereby reducing the fabrication cost. The CMUT used in this thesis is fabricated using the nitride-oxide bonding technique described in [23].

Chapter 6

Testing and Characterization of Capacitive Micromachined Ultrasound Transducers

6.1 Parameters of Capacitive Micromachined Ultrasound Transducers

The CMUTs used in this thesis were fabricated with the nitride-to-oxide wafer bonding method. Two pieces <100> silicon wafer were used for the top and bottom wafer. Silicon nitride was deposited on the top wafer with the low-pressure chemical vapor deposition (LPCVD) process to form the membrane of the CMUTs. The insulator was made with a layer of silicon dioxide that was thermally grown on the bottom wafer. A diagram of the CMUT is shown in figure 6.1. The parameters of the fabricated are listed in table 5.

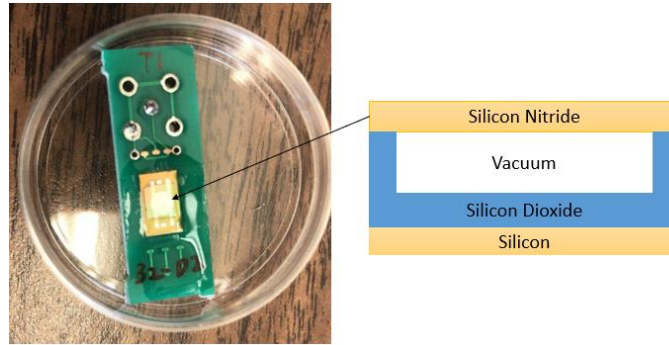


Figure 6.1 Diagram of CMUT used in the experiments

Table 5 Parameters of fabricated CMUTs

Parameters	Dimensions
Membrane Thickness (nm)	520
Membrane Diameter (μm)	25
Cavity Depth (nm)	180
Insulator Thickness (nm)	310

6.2 Characterization of Electrical Impedance

The resonance frequency of the CMUT in air was first characterized by measuring the electrical impedance while sweeping the modulation frequency. A bias tee (PSPL5530B, Tektronix) was used to combine the DC voltages and the vector network analyzer (VNA, TTR503a, Tektronix) to actuate and measure the S11 parameter. S11 parameter is the reflection coefficient of the input port of the electrical system. With equation (6.1), the measured S11 parameter can be converted to the electrical impedance of the CMUT. Figure 6.2 shows the schematic of the experimental set-up for characterizing the electrical impedance. At resonance frequency, there will be minimal energy that will be reflected back to the vector network analyzer as most of the energy is converted to mechanical motion of the membrane. The resonance frequency of the CMUT is evident with the sudden dip in electrical impedance at a specific frequency, which is the resonance frequency. The resonance frequency for this CMUT was found to be approximately 11.59 MHz. From figure 6.3, it can be observed that due to the spring softening effect, there is a decrease in resonance frequency as the applied DC voltage increases.

$$Z_L = Z_0 \left(\frac{1 + S_{11}}{1 - S_{11}} \right) \quad (6.1)$$

where $Z_0 = 50 \Omega$ and Z_L is the load impedance of the device under test which in this case is the electrical impedance of the CMUT

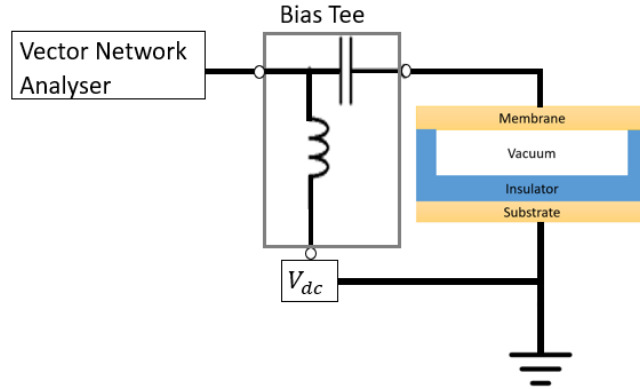
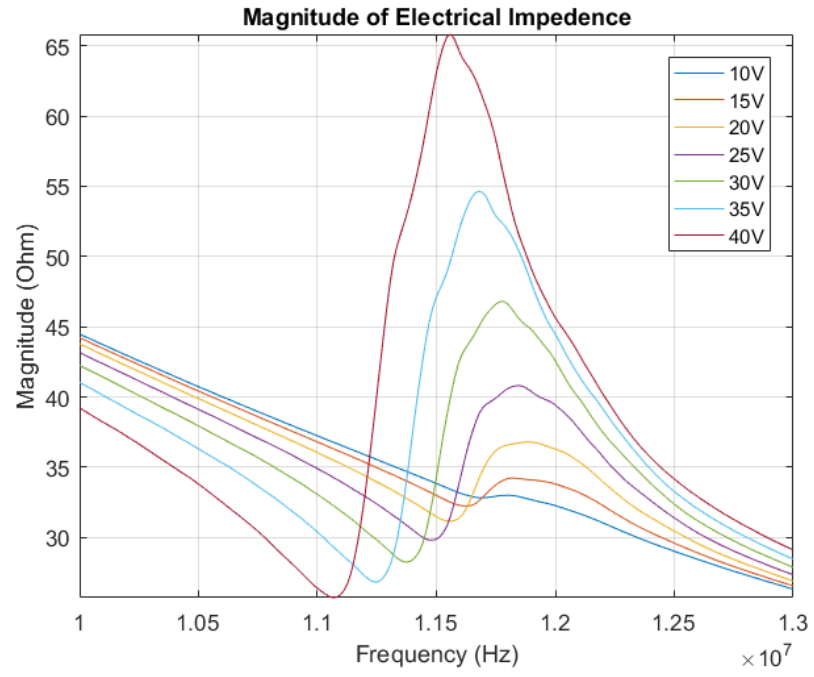


Figure 6.2 Schematic of the experimental set-up for characterization of electrical impedance

(a)



(b)

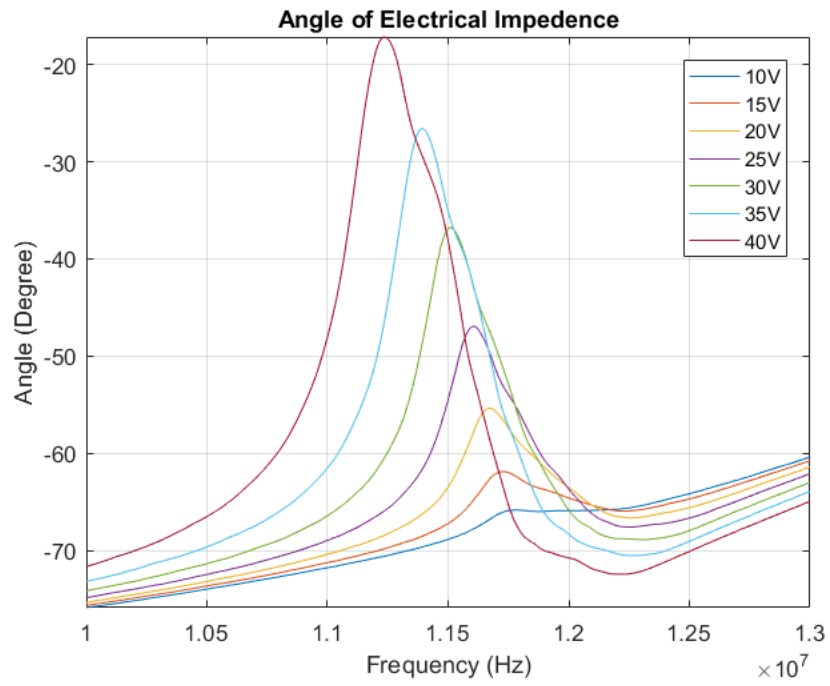


Figure 6.3 The electrical impedance of CMUT-R in (a) magnitude and (b) phase

6.3 Characterization of Receive Sensitivity

Transmission Experiment

The receive sensitivity is an important parameter in understanding the performance of the detectors in PAI. In order to test the receive sensitivity of the CMUT used for PAI, CMUT-R, a pitch-catch experiment was conducted. A CMUT, CMUT-T, with a similar design specification was used to transmit the signal. Both CMUT-T and the hydrophone (HGL-0200, Onda) were submerged into vegetable oil for better acoustic coupling. CMUT-T. was driven by a commercial pulser (NDT 5073PR, Panametrics) and a 25V DC applied bias. Figure 6.4 shows an experimental set-up of the transmission test. The maximum signal was achieved by adjusting the three-axis stage so that the CMUT-T is aligned to the center of the hydrophone. Using the time of flight and with the estimated speed of sound in oil as 1470 m/s, the calculated distance is approximately 11 mm. The time-domain of the CMUT-T is reflected on the oscilloscope through the 20-dB pre-amplifier (Onda AH-2010) which was connected to the hydrophone as shown in figure 6.5. The corresponding frequency spectrum was obtained using the Fourier Transform and shown in figure 6.6.

As previously explained, due to the damping caused by oil immersion, with an applied DC voltage of 25V, the center frequency of CMUT-T is shifted from 13.54 MHz in air to 5.08 MHz when immersed in oil. The voltage output obtained was 95.41 mVpp. Using the hydrophone's calibration sensitivity datasheet, 0.33mV/kPa at 5.05 MHz, the output pressure from CMUT-T is found to be 289.13kPa.

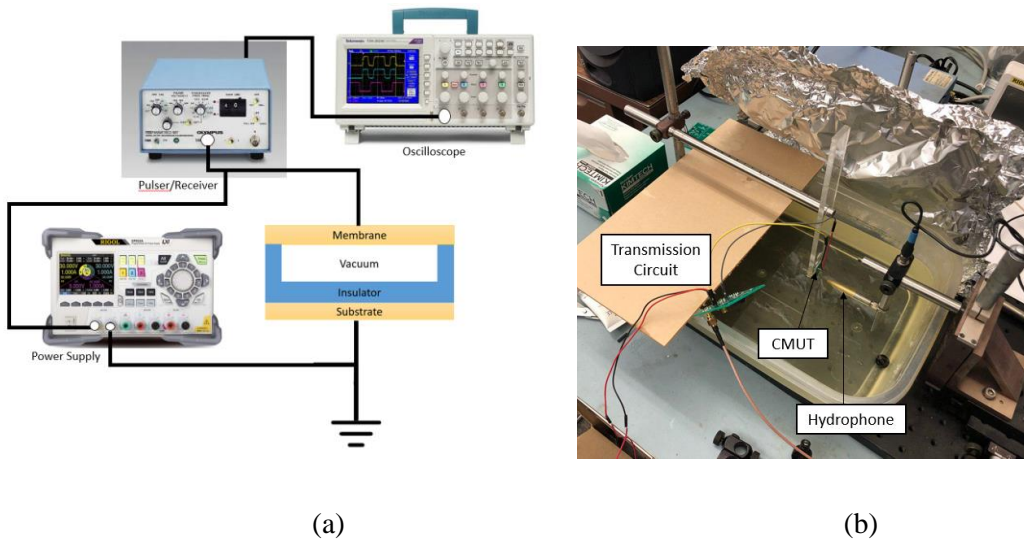


Figure 6.4 (a) Circuit and (b) Experimental set-up of the transmission test

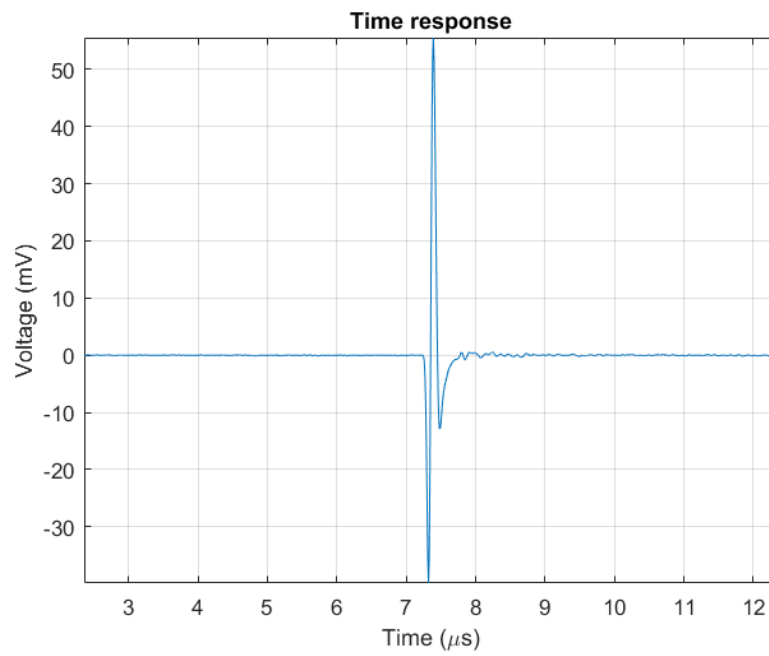


Figure 6.5 Graph of Time response of CMUT-T in transmission

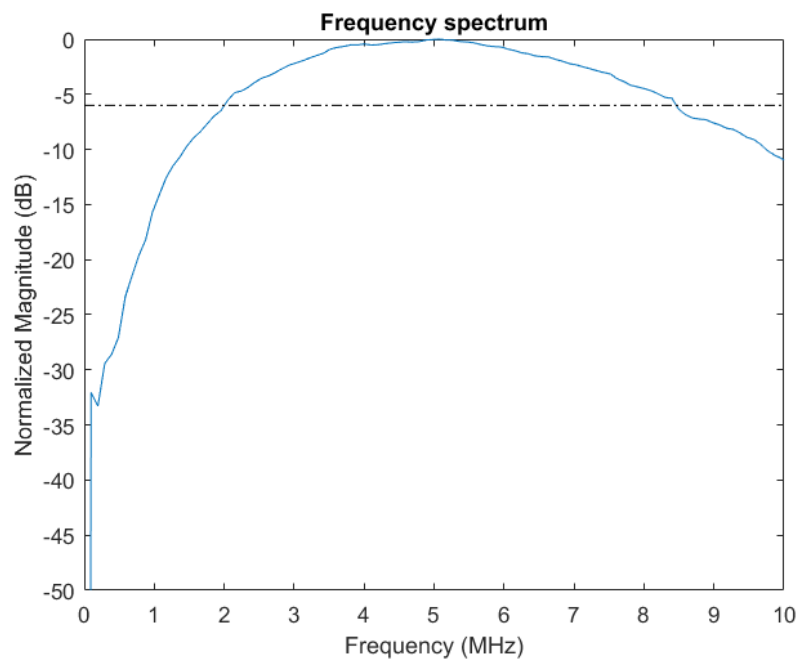


Figure 6.6 Frequency spectrum of CMUT-T in transmission mode

Receive Sensitivity Experiment

For the receive sensitivity experiment, the hydrophone was replaced with CMUT-R while the distance and alignment were kept constant. A transimpedance amplifier made with an operational amplifier (OPA354, Texas Instruments Inc), a $10\text{ k}\Omega$ feedback resistor and a 0.6 pF capacitor, was used to amplify and convert the received signal to voltage. A schematic of the circuit set-up is shown in figure 6.7. With a bias voltage of 30 V , the output voltage from CMUT-R was determined to be 1.47 V_{pp} . The time response of the signal and its corresponding frequency spectrum is shown in figure 6.8 and figure 6.9. The center frequency and - 6-db fractional bandwidth of CMUT-R in immersion were found to be 3.47 MHz and 102% respectively.

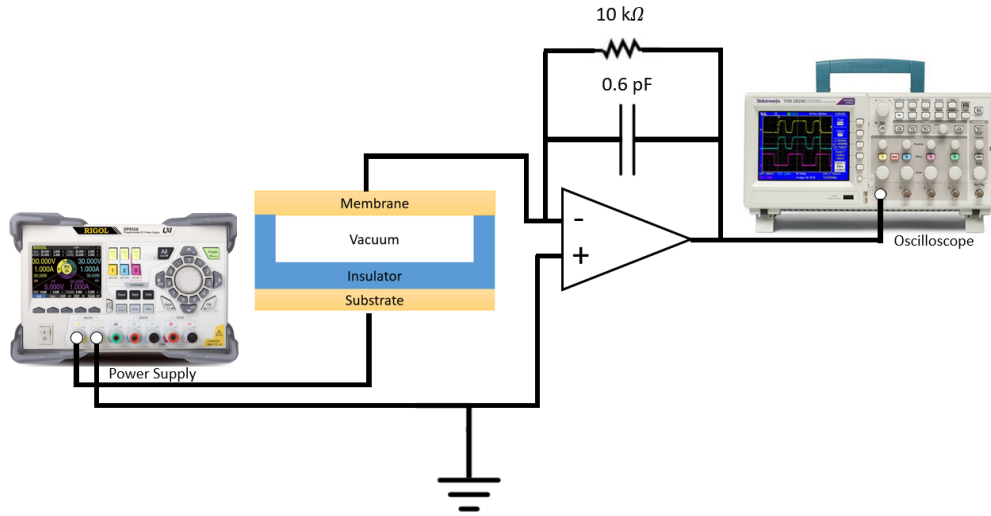


Figure 6.7 Circuit set-up of CMUT-R

From the results obtained with the transmission and receiving tests, the receive sensitivity of CMUT-R was calculated to be 5.09 mV/KPa . The receive sensitivity is a little on the lower end. This can be due to the difference in the center frequency of both CMUT-T and CMUT-R. Thus, the receive sensitivity of CMUT-R can be improved if a transducer with center frequency closer to CMUT-R was chosen for the experiment. However, this would not be an issue for PAI. In PAI application, photoacoustic signals have a broad bandwidth. Therefore, CMUT-R might be able to achieve a higher receive sensitivity than what is reported in this thesis.

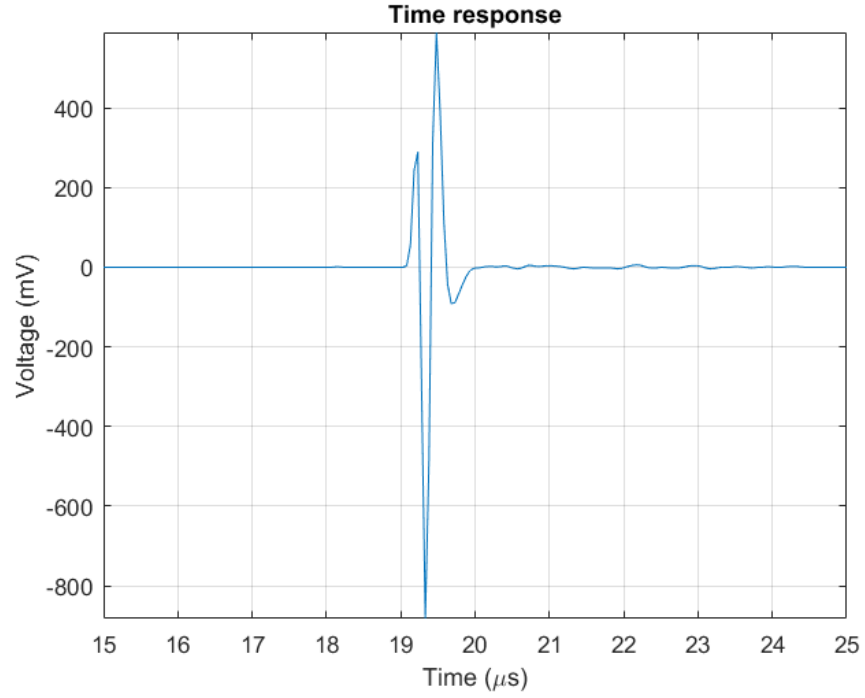


Figure 6.8 Time response of CMUT-R in receiving mode

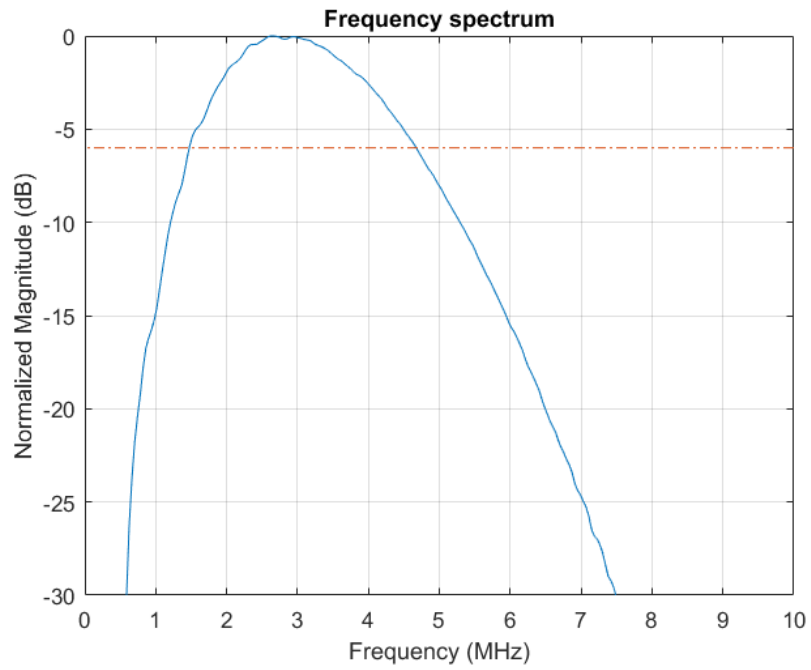


Figure 6.9 Frequency Response of CMUT-R in receive mode

6.4 Summary

The nitride-to-oxide wafer-bonded CMUTs was characterized both in air and immersion. The performance of the CMUT coincides with its design where the theoretical analysis results from numerical and finite element analysis are similar to the experimental results as shown in table 6. Apart from the general advantages of CMUTs such as being CMOS compatible and the ability to be easily fabricated into an array, the nitride-to-oxide wafer-bonded CMUTs can be a good detector for PAI with good cell to cell uniformity, the reduced cost and complexity of the fabrication process [23], [110]. With the limited availability and the high cost of SOI wafer, the nitride membrane can be a good alternative for wafer bonded CMUTs. In applications such as AR-PAM, the lateral resolution is dependent on the center frequency of the transducer. Thus, one of the future improvements to enhance the image quality for AR-PAM application would be to fabricate CMUTs with higher center frequency.

Table 6 Comparison of CMUTs' center frequency and bandwidth from theoretical and experimental results

	Numerical Analysis	Finite Element Analysis	Experimental Result
In-Air	11.518 MHz	11.20 MHz	11.59 MHz
In-immersion	3.489 MHz	3.67 MHz	3.47 MHz

Chapter 7

Summary and Future Work

7.1 Summary

In this work, various photoacoustic imaging techniques ranging from contact to non-contact based detection mechanisms were explored and investigated. Photoacoustic imaging of carbon fiber with OR-PAM method was captured with both a piezoelectric transducer and the PARS mechanism. Since the resolution with OR-PAM imaging is dependent on the optical focus, both detection techniques produce similar results. Thus, the selection of the detector lies in its application where piezoelectric transducer provides a better penetration depth which will be useful in applications such as AR-PAM and PACT while PARS mechanism provides a non-contact form of imaging. In the subsequent chapters, the basic operating principles and design parameters of CMUTs were studied with numerical and finite element analysis. For contact-based detection, CMUTs are a better option as compared to piezoelectric transducers. They do not require a coupling layer and have a larger fractional bandwidth. This will allow the production of high-quality images with a miniaturized detector. Furthermore, being CMOS compatible, CMUTs can also be integrated with CMOS, which can help to maximize SNR so as to further enhance image quality. In Chapter 6 of this thesis, the CMUT fabricated with nitride-to-oxide wafer bonding technology was characterized. The 3.47 MHz CMUT was able to achieve a receive sensitivity of 5.09 mv/kPa.

7.2 Future Work

7.2.1 Industrialization of Capacitive Micromachined Ultrasound Transducer for Photoacoustic Imaging

CMUTs for photoacoustic imaging has been industrialized. Currently, Canon is rolling out its 3D real-time photoacoustic mammogram into the market. Canon has worked with Kyoto University in developing this system with experimental testing and clinical trials which can be found in research papers produced by the group. Asao et al. [120] had built a prototype of the photoacoustic mammogram with a CMUT-based receiver called PAM-02. A piezoelectric transducer was used in their initial prototype, PAM-01, but to increase the system's imaging sensitivity, the team replaced it with a CMUT receiver. A more recent clinical trial was done with another of their prototype, PAI-04 [132]. PAI-04

is similar to its predecessor, PAI-03 with the addition of an ultrasound imaging system. PAI-04 was able to image the arterioles and venules of the palm, thigh, and breast with 500 4 MHz CMUT elements as the receiver. This is reportedly the first imaging done for tumor-related blood vessels in human cancer tissue that can achieve such fine details.

7.2.2 Challenges and Prospects of Using Capacitive Micromachined Ultrasound Transducer for Photoacoustic Imaging

Like many other micro-electro-mechanical systems (MEMS) devices, CMUTs also face the issue of dielectric charging where the built-up of charges causes the center frequency to be shifted [95]. This affects the performance of CMUTs and can potentially cause them to breakdown. Some proposed solutions to resolve this issue includes replacing the insulation layer with an insulator post [133], extending the insulation layer [134], and having a spacer below the membrane [135]. One of CMUTs' main structure is the micron-scale thin membrane which can be easily damaged if it is not well protected. Encapsulation helps to minimize the damage, but there is a trade-off as a thicker encapsulation layer causes more acoustic attenuation which reduces CMUTs' efficiency [95]. Another challenge that CMUT arrays face is crosstalk. Since the elements are placed on the same substrate, the vibration of one CMUT element inevitably affects the neighboring elements [95]. These unwanted vibrations result in the production of noise henceforth impairing the image quality. Researchers have been exploring various solutions to address the issue of crosstalk using device modeling [136] and also programmable waveforms [137]

With all the challenges and limitations of CMUT technology, the prospects of using CMUTs for PAI is promising. The ability to make a flexible CMUT array is another untapped domain for the future development of CMUTs for PAI. Besides being able to conform to different geometries, a flexible device can also provide a larger FOV for imaging applications. For future development of CMUTs in PAI applications, one crucial aspect is to attain higher resolution imaging with higher frequency CMUTs. Another area to explore is the advancement of CMUTs for real-time 3D PAI applications. Even though 2D CMUT arrays have been fabricated, most results thus far have still relied on mechanically scanning. Operating a 2D CMUT array system without requiring this mechanical scanning may help to further push CMUTs in the direction of real-time 3D PAI applications. The ability

to make a flexible CMUT array is another untapped domain for the future development of CMUTs for PAI. Besides being able to conform to different geometries, a flexible device can also provide a larger FOV for imaging applications. Various groups have shown the fabrication and potential application of flexible 2D CMUT arrays for ultrasound imaging [108], [138], [139]. A flexible CMUT would provide a strong candidate when compared with other techniques for MIS application where a small active area and large FOV is needed. It will also be immensely useful in large FOV PACT applications such as the imaging of the brain [25], [47], [48] and breast cancer [50] or a virtual point transducer to enhance the FOV further and potentially reduce the SNR [27].

Bibliography

- [1] J. Buchmann *et al.*, “Characterization and modeling of Fabry–Perot ultrasound sensors with hard dielectric mirrors for photoacoustic imaging,” *Appl. Opt.*, vol. 56, no. 17, p. 5039, 2017.
- [2] S. Ashkenazi, Y. Hou, T. Buma, and M. O’Donnell, “Optoacoustic imaging using thin polymer etalon,” *Appl. Phys. Lett.*, vol. 86, no. 13, pp. 1–3, 2005.
- [3] S. Huang, S. Chen, T. Ling, A. Maxwell, S. ASHKENAZI, and L. J. GUO, “Optical Detection of High-Frequency Ultrasound Using Polymer Microring Resonators,” in *1st International Symposium on Laser Ultrasonics: Science, Technology and Applications*, 2008.
- [4] H. Li, B. Dong, Z. Zhang, H. F. Zhang, and C. Sun, “A transparent broadband ultrasonic detector based on an optical micro-ring resonator for photoacoustic microscopy,” *Sci. Rep.*, vol. 4, p. 4496, 2014.
- [5] B. Dong, S. Chen, Z. Zhang, C. Sun, and H. F. Zhang, “Photoacoustic probe using a micro-ring resonator ultrasonic sensor for endoscopic applications,” *Opt. Lett.*, vol. 39, no. 15, pp. 4372–4375, 2014.
- [6] Y. Cao, K. Ha, M. Kim, H. Kang, J. Oh, and J. Kim, “A circular array transducer for photoacoustic imaging by using piezoelectric single crystal lead magnesium niobate – lead zirconate titanate,” *Jpn. J. Appl. Phys.*, vol. 54, no. 7S1, p. 07HD08, 2015.
- [7] P. Hajireza, W. Shi, K. Bell, R. J. Paproski, and R. J. Zemp, “Non-interferometric photoacoustic remote sensing microscopy,” *Light Sci. Appl.*, vol. 6, no. 6, pp. e16278-8, 2017.
- [8] S. Abbasi *et al.*, “All-optical Reflection-mode Microscopic Histology of Unstained Human Tissues,” *Sci. Rep.*, no. June, pp. 1–11, 2019.
- [9] I. O. Wygant, X. Zhuang, P. S. Kuo, D. T. Yeh, O. Oralkan, and B. T. Khuri-Yakub, “Photoacoustic imaging using a two-dimensional CMUT array,” in *IEEE Ultrasonics Symposium*, 2005, vol. 4, pp. 1921–1924.
- [10] S. Vaithilingam *et al.*, “Three-dimensional photoacoustic imaging using a two-dimensional CMUT array,” *IEEE Trans. Ultrason. Ferroelectr. Freq. Control*, vol. 56, no. 11, pp. 2411–2419, 2009.
- [11] S. Kothapalli, T. Ma, S. Vaithilingam, B. T. Khuri-yakub, and S. S. Gambhir, “Deep Tissue Photoacoustic Imaging Using a Miniaturized 2-D Capacitive Micromachined Ultrasonic

- Transducer Array,” *IEEE Trans. Biomed. Eng.*, vol. 59, no. 5, pp. 1199–1204, 2012.
- [12] R. K. W. Chee, A. Sampaleanu, D. Rishi, and R. J. Zemp, “Top Orthogonal to Bottom Electrode (TOBE) 2-D CMUT Arrays for 3-D Photoacoustic Imaging,” *IEEE Trans. Ultrason. Ferroelectr. Freq. Control*, vol. 61, no. 8, pp. 1393–1395, 2014.
 - [13] J. Chen, M. Wang, J. Cheng, Y. Wang, P. Li, and S. Member, “A Photoacoustic Imager With Light Illumination Through an Infrared-Transparent Silicon CMUT Array,” *IEEE Trans. Ultrason. Ferroelectr. Freq. Control*, vol. 59, no. 4, pp. 766–775, 2012.
 - [14] X. Zhang, X. Wu, O. J. Adelegan, F. Y. Yamaner, and O. Oralkan, “Backward-Mode Photoacoustic Imaging Using Illumination Through a CMUT with Improved Transparency,” *IEEE Trans. Ultrason. Ferroelectr. Freq. Control*, vol. 65, no. 1, pp. 85–94, 2018.
 - [15] Z. Li, A. Ilkhechi, and R. Zemp, “Transparent capacitive micromachined ultrasonic transducers (CMUTs) for photoacoustic applications,” *Opt. Express*, vol. 27, no. 9, pp. 13204–13218, 2019.
 - [16] R. K. W. Chee, P. Zhang, M. Maadi, and R. J. Zemp, “Multifrequency interlaced CMUTs for photoacoustic imaging,” *IEEE Trans. Ultrason. Ferroelectr. Freq. Control*, vol. 64, no. 2, pp. 391–401, 2017.
 - [17] J. Zhang *et al.*, “Development of a multi-band photoacoustic tomography imaging system based on a capacitive micromachined ultrasonic transducer array,” *Appl. Opt.*, vol. 56, no. 14, pp. 4012–4018, 2017.
 - [18] S. H. Pun *et al.*, “Monolithic Multiband CMUTs for Photoacoustic Computed Tomography with In Vivo Biological Tissue Imaging,” *IEEE Trans. Ultrason. Ferroelectr. Freq. Control*, vol. 65, no. 3, pp. 465–475, 2018.
 - [19] X. Cheng, J. Chen, and C. Li, “A miniature capacitive micromachined ultrasonic transducer array for minimally invasive photoacoustic imaging,” *J. Microelectromechanical Syst.*, vol. 19, no. 4, pp. 1002–1011, 2010.
 - [20] A. Nikoozadeh *et al.*, “Photoacoustic imaging using a 9F microLinear CMUT ICE catheter,” in *IEEE International Ultrasonics Symposium (IUS)*, 2012, pp. 24–27.
 - [21] S. Vaithilingam *et al.*, “Tomographic photoacoustic imaging using capacitive micromachined

- ultrasonic transducer (CMUT) technology,” in *IEEE Ultrasonics Symposium*, 2006, pp. 397–400.
- [22] A. Nikoozadeh *et al.*, “An integrated Ring CMUT array for endoscopic ultrasound and photoacoustic imaging,” in *IEEE International Ultrasonics Symposium, IUS*, 2013, pp. 1178–1181.
 - [23] A. I. H. Chen, L. L. P. Wong, and J. T. W. Yeow, “Practical CMUT Fabrication With a Nitride-to-Oxide-Based Wafer Bonding Process,” *J. Microelectromechanical Syst.*, vol. 26, no. 4, pp. 829–836, 2017.
 - [24] X. Wang, W. W. Roberts, P. L. Carson, D. P. Wood, and J. B. Fowlkes, “Photoacoustic tomography : a potential new tool for prostate cancer,” *Biomed. Opt. Express*, vol. 1, no. 4, pp. 770–775, 2010.
 - [25] P. Zhang *et al.*, “High-resolution deep functional imaging of the whole mouse brain by photoacoustic computed tomography in vivo,” *J. Biophotonics*, vol. 11, no. 1, pp. 1–6, 2018.
 - [26] I. Y. Petrova, Y. Y. Petrov, R. O. Esenaliev, D. J. Deyo, I. Cicinaite, and D. S. Prough, “Noninvasive monitoring of cerebral blood oxygenation in ovine superior sagittal sinus with novel multi-wavelength optoacoustic system,” *Opt. Express*, vol. 17, no. 9, pp. 221–229, 2009.
 - [27] L. Nie, Z. Guo, and L. V Wang, “Photoacoustic tomography of monkey brain using virtual point ultrasonic transducers,” *J. Biomed. Opt.*, vol. 16, no. 7, 2011.
 - [28] Z. Chen *et al.*, “Non-invasive multimodal optical coherence and photoacoustic tomography for human skin imaging,” *Sci. Rep.*, vol. 7, pp. 1–11, 2017.
 - [29] J.-T. Oh, M.-L. Li, H. F. Zhang, K. Maslov, G. Stoica, and L. V. Wang, “Three-dimensional imaging of skin melanoma in vivo by dual-wavelength photoacoustic microscopy,” *J. Biomed. Opt.*, vol. 11, no. 3, pp. 1–4, 2006.
 - [30] S. Jiao *et al.*, “Photoacoustic ophthalmoscopy for in vivo retinal imaging,” *Opt. Express*, vol. 18, no. 4, pp. 3967–3972, 2010.
 - [31] L. V Wang, “Prospects of photoacoustic tomography,” *Med. Phys.*, vol. 35, no. 12, pp. 5758–5767, 2008.
 - [32] M. Xu and L. V. Wang, “Photoacoustic imaging in biomedicine,” *Rev. Sci. Instrum.*, vol. 77,

no. 4, 2006.

- [33] P. Beard, “Biomedical Photoacoustic Imaging,” *Interface Focus*, vol. 1, pp. 602–631, 2011.
- [34] S. Y. Emelianov, P. C. Li, and M. O’Donnell, “Photoacoustics for molecular imaging and therapy,” *Phys. Today*, vol. 62, no. 8, pp. 34–39, 2009.
- [35] L. V Wang and J. Yao, “A practical guide to photoacoustic tomography in the life sciences,” *Nat. Methods*, vol. 13, no. 8, p. 267, 2016.
- [36] V. W. Lihong and G. Liang, “Photoacoustic microscopy and computed tomography: from bench to bedside,” *Annu. Rev. Biomed. Eng.*, vol. 16, no. 7, pp. 155–185, 2014.
- [37] Y. Zhou, J. Yao, and L. V. Wang, “Tutorial on photoacoustic tomography,” *J. Biomed. Opt.*, vol. 21, no. 6, p. 061007, 2016.
- [38] J. Xia, J. Yao, and L. Wang, “Photoacoustic tomography: Principles and advances,” *Electromagn. waves (Cambridge, Mass.)*, vol. 147, pp. 1–22, 2014.
- [39] M. Li, Y. Tang, and J. Yao, “Photoacoustic tomography of blood oxygenation: A mini review,” *Photoacoustics*, vol. 10, pp. 65–73, 2018.
- [40] J. Yao and L. V. Wang, “Sensitivity of photoacoustic microscopy,” *Photoacoustics*, vol. 2, pp. 87–101, 2014.
- [41] J. Yao and L. V Wang, “Photoacoustic microscopy,” *Laser & Photonics*, vol. 7, no. 5, pp. 758–778, 2013.
- [42] L. V. Wang and S. Hu, “Photoacoustic Tomography: In Vivo Imaging , from Organelles to Organs,” *Science (80-.)*, vol. 335, no. 6075, pp. 1458–1462, 2012.
- [43] J. Xia, K. Chatni, Muhammad R. Maslov, Z. Guo, K. Wang, M. Anastasio, and L. V. Wang, “Whole-body ring-shaped confocal photoacoustic computed tomography of small animals in vivo,” *J. Biomed. Opt.*, vol. 17, no. 5, p. 050506, 2012.
- [44] Y. Xu and L. V Wang, “Time Reversal and Its Application to Tomography with Diffracting Sources,” *Phys. Rev. Lett.*, vol. 92, no. 3, p. 033902, 2004.
- [45] B. E. Treeby, E. Z. Zhang, and B. T. Cox, “Photoacoustic tomography in absorbing acoustic media using time reversal,” *Inverse Probl.*, vol. 26, no. 11, p. 115003, 2010.

- [46] J. Yuan *et al.*, “Real-time photoacoustic and ultrasound dual-modality imaging system facilitated with graphics processing unit and code parallel optimization,” *J. Biomed. Opt.*, vol. 18, no. 8, pp. 086001–086001, 2013.
- [47] J. Yao *et al.*, “Noninvasive photoacoustic computed tomography of mouse brain metabolism in vivo,” *Neuroimage*, vol. 64, pp. 257–266, 2013.
- [48] W. Li *et al.*, “In Vivo Photoacoustic Imaging of Brain Injury and Rehabilitation by High-Efficient Near-Infrared Dye Labeled Mesenchymal Stem Cells with Enhanced Brain Barrier Permeability,” *Adv. Sci.*, vol. 5, no. 2, p. 1700277, 2018.
- [49] J. Lv *et al.*, “Hemispherical photoacoustic imaging of myocardial infarction : in vivo detection and monitoring,” *Eur. Radiol.*, vol. 28, no. 5, pp. 2176–2183, 2018.
- [50] L. Lin *et al.*, “Single-breath-hold photoacoustic computed tomography of the breast,” *Nat. Communications*, vol. 9, no. 2352, 2018.
- [51] Y. Liu, L. Fu, M. Xu, J. Zheng, and Z. Yuan, “Dual-Modal In Vivo Fluorescence/Photoacoustic Microscopy Imaging of Inflammation Induced by GFP-Expressing Bacteria,” *Sensors (Switzerland)*, vol. 19, no. 2, p. 238, 2019.
- [52] S. Hu and L. V. Wang, “Photoacoustic imaging and characterization of the microvasculature,” *J. Biomed. Opt.*, vol. 15, no. 1, pp. 1–15, 2010.
- [53] V. Periyasamy, N. Das, A. Sharma, and M. Pramanik, “1064 nm acoustic resolution photoacoustic microscopy,” *J. Biophotonics*, no. September, pp. 1–9, 2018.
- [54] S. Mallidi, G. P. Luke, and S. Emelianov, “Photoacoustic imaging in cancer detection , diagnosis , and treatment guidance,” *Trends Biotechnol.*, vol. 29, no. 5, pp. 213–221, 2011.
- [55] S. Park, C. Lee, J. Kim, and C. Kim, “Acoustic Resolution Photoacoustic Microscopy,” *Biomed. Eng. Lett.*, vol. 4, no. 3, pp. 213–222, 2014.
- [56] J. Koo *et al.*, “In vivo non-ionizing photoacoustic mapping of sentinel lymph nodes and bladders with ICG- enhanced carbon nanotubes,” *Phys. Med. Biol.*, vol. 57, no. 23, pp. 7853–7862, 2012.
- [57] C. Kim, M. Jeon, and L. V Wang, “Nonionizing photoacoustic cystography in vivo,” *Opt. Lett.*, vol. 36, no. 18, pp. 3599–3601, 2011.

- [58] Y. Zhang *et al.*, “Non-invasive multimodal functional imaging of the intestine with frozen micellar naphthalocyanine,” *Nat. Nanotechnol.*, vol. 9, no. 8, pp. 631–638, 2014.
- [59] S. L. Chen, L. J. Guo, and X. Wang, “All-optical photoacoustic microscopy,” *Photoacoustics*, vol. 3, no. 4, pp. 143–150, 2015.
- [60] S. Hu and L. V Wang, “Optical-Resolution Photoacoustic Microscopy : Auscultation of Biological Systems at the Cellular Level,” *Biophys. J.*, vol. 105, no. 4, pp. 841–847, 2013.
- [61] T. Liu, Q. Wei, W. Song, J. M. Burke, and S. Jiao, “Near-infrared light photoacoustic ophthalmoscopy,” *Biomed. Opt. Express*, vol. 3, no. 4, pp. 1169–1176, 2012.
- [62] S. Hu, B. Rao, K. Maslov, and L. V Wang, “Label-free Photoacoustic Ophthalmic Angiography,” *Opt. Lett.*, vol. 35, no. 1, pp. 1–3, 2010.
- [63] Y. Zhou, W. Xing, K. I. Maslov, L. A. Cornelius, and L. V Wang, “Handheld photoacoustic microscopy to detect melanoma depth in vivo,” *Opt. Lett.*, vol. 39, no. 16, pp. 4731–4734, 2014.
- [64] S. Hu, K. Maslov, V. Tsytarev, and L. V. Wang, “Functional transcranial brain imaging by optical-resolution photoacoustic microscopy,” *J. Biomed. Opt.*, vol. 14, no. 4, pp. 1–9, 2009.
- [65] Y. Liu, L. Nie, and X. Chen, “Photoacoustic Molecular Imaging: From Multiscale Biomedical Applications Towards Early-Stage Theranostics,” *Trends Biotechnol.*, vol. 34, no. 5, p. 420, 2016.
- [66] H. Brecht, R. Su, M. Fronheiser, S. A. Ermilov, A. Conjusteau, and A. A. Oraevsky, “Whole-body three-dimensional optoacoustic tomography system for small animals,” *J. Biomed. Opt.*, vol. 14, no. 6, pp. 1–8, 2009.
- [67] M. Erfanzadeh and Q. Zhu, “Photoacoustics Photoacoustic imaging with low-cost sources ; A review,” *Photoacoustics*, vol. 14, pp. 1–11, 2019.
- [68] S. Hu, K. Maslov, and L. V Wang, “Photoacoustic Microscopy,” 2013.
- [69] H. F. Zhang, K. Maslov, G. Stoica, and L. V Wang, “Functional photoacoustic microscopy for high-resolution and noninvasive in vivo imaging,” *Nat. Biotechnol.*, vol. 24, no. 7, pp. 848–851, 2006.

- [70] K. Meyer, N. Muller, Z. Liu, and T. Pfeifer, “Temporal resolution beyond the average pulse duration in shaped noisy-pulse transient absorption spectroscopy,” *Appl. Opt.*, vol. 55, no. 36, pp. 10318–10322, 2016.
- [71] K. Irisawa, T. Hirasawa, K. Hirota, K. Tsujita, and M. Ishihara, “Influence of laser pulse width to the photoacoustic temporal waveform and the image resolution with a solid- state excitation laser,” in *Photons Plus Ultrasound: Imaging and Sensing 2012*, 2012, no. 8223.
- [72] G. Wissmeyer, M. A. Pleitez, A. Rosenthal, and V. Ntziachristos, “Looking at sound : optoacoustics with all-optical ultrasound detection,” *Light Sci. Appl.*, vol. 7, no. 53, 2018.
- [73] J. Chen, “Capacitive micromachined ultrasonic transducer arrays for minimally invasive medical ultrasound,” *J. Micromechanics Microengineering*, vol. 20, no. 2, p. 023001, 2010.
- [74] B. H. Lee *et al.*, “Interferometric Fiber Optic Sensors,” *Sensors (Switzerland)*, vol. 12, no. 3, pp. 2467–2486, 2012.
- [75] B. Dong, C. Sun, and H. F. Zhang, “Optical Detection of Ultrasound in Photoacoustic Imaging,” *IEEE Trans Biomed Eng.*, vol. 64, no. 1, pp. 4–15, 2017.
- [76] P. Hajireza, K. Krause, M. Brett, and R. Zemp, “Glancing angle deposited nanostructured film Fabry-Perot etalons for optical detection of ultrasound,” *Opt. Express*, vol. 21, no. 5, pp. 6391–6400, 2013.
- [77] P. Hajireza, J. Sorge, M. Brett, and R. J. Zemp, “In vivo optical resolution photoacoustic microscopy using glancing angle-deposited nanostructured Fabry–Perot etalons,” *Opt. Lett.*, vol. 40, no. 7, pp. 1350–1353, 2015.
- [78] R. Ansari, E. Z. Zhang, and A. E. Desjardins, “All-optical forward-viewing photoacoustic probe for high-resolution 3D endoscopy,” *Light Sci. Appl.*, vol. 7, no. 75, 2018.
- [79] A. A. Plumb, N. T. Huynh, J. Guggenheim, E. Zhang, and P. Beard, “Rapid volumetric photoacoustic tomographic imaging with a Fabry-Perot ultrasound sensor depicts peripheral arteries and microvascular vasomotor responses to thermal stimuli,” *Eur. Radiol.*, vol. 28, no. 3, pp. 1037–1045, 2018.
- [80] M. W. Schellenberg and H. K. Hunt, “Hand-held optoacoustic imaging: A review,” *Photoacoustics*, vol. 11, no. June, pp. 14–27, 2018.

- [81] M. R. Islam, M. M. Ali, M. Lai, K. Lim, and H. Ahmad, "Chronology of Fabry-Perot Interferometer Fiber-Optic Sensors and Their Applications: A Review," *Sensors (Switzerland)*, vol. 14, no. 4, pp. 7451–7488, 2014.
- [82] S. Katzir, "The Discovery of the Piezoelectric Effect," in *Archive for History of Exact Sciences*, vol. 57, 2003, pp. 61–91.
- [83] M. Wegener, H. Oehler, D. Lellinger, and I. Alig, "Note : Piezoelectric polymers as transducers for the ultrasonic-reflection method and the application in mechanical property-screening of coatings," *Rev. Sci. Instrum.*, vol. 83, no. 1, p. p.016102, 2012.
- [84] Y. Xin, X. Li, H. Tian, C. Guo, C. Qian, and S. Wang, "Shoes-equipped piezoelectric transducer for energy harvesting : A brief review," *Ferroelectrics*, vol. 493, no. 1, pp. 12–24, 2016.
- [85] A. Raihan, M. Siddique, S. Mahmud, and B. Van Heyst, "A comprehensive review on vibration based micro power generators using electromagnetic and piezoelectric transducer mechanisms," *Energy Convers. Manag.*, vol. 106, pp. 728–747, 2015.
- [86] K. K. Shung, J. M. Cannata, and Q. F. Zhou, "Piezoelectric materials for high frequency medical imaging applications : A review," *J. Electroceramics*, vol. 19, no. 1, pp. 139–145, 2007.
- [87] K. H. Martin *et al.*, "Dual-Frequency Piezoelectric Transducers for Contrast Enhanced Ultrasound Imaging," *Sensors (Switzerland)*, vol. 14, pp. 20825–20842, 2014.
- [88] I. Akiyama, N. Yoshizumi, S. Saito, Y. Wada, D. Koyama, and K. Nakamura, "Development of Multiple-Frequency Ultrasonic Imaging System Using Multiple Resonance Piezoelectric Transducer," *Jpn. J. Appl. Phys.*, vol. 51, no. 7, p. 07GF02, 2012.
- [89] S. MANOHAR and D. RAZANSKY, "Photoacoustics : a historical review," *Adv. Opt. Photonics*, vol. 8, no. 4, pp. 586–617, 2016.
- [90] M. Vallet *et al.*, "Quantitative comparison of PZT and CMUT probes for photoacoustic imaging: Experimental validation," *Photoacoustics*, vol. 8, pp. 48–58, 2017.
- [91] A. Dangi, S. Agrawal, J. Lieberknecht, J. Zhang, and S. Kothapalli, "Ring Ultrasound Transducer based Miniaturized Photoacoustic Imaging System," in *IEEE SENSORS*, 2018, pp.

1–4.

- [92] G. Paltauf, P. Hartmair, G. Kovachev, and R. Nuster, “Piezoelectric line detector array for photoacoustic tomography,” *Photoacoustics*, vol. 8, pp. 28–36, 2017.
- [93] J. Yang *et al.*, “A 2.5-mm diameter probe for photoacoustic and ultrasonic endoscopy,” *Opt. Express*, vol. 20, no. 21, pp. 23944–23953, 2012.
- [94] K. Maslov, H. F. Zhang, S. Hu, and L. V Wang, “Optical-resolution photoacoustic microscopy for in vivo imaging of single capillaries,” *Opt. Lett.*, vol. 33, no. 9, pp. 929–931, 2008.
- [95] A. I. H. Chen, L. L. P. Wong, and J. T. W. Yeow, “Recent advances in capacitive micromachined ultrasonic transducer imaging systems,” *Med. Imaging Technol. Appl.*, pp. 253–271, 2013.
- [96] C. Liu, Q. Zhou, F. T. Djuth, and K. K. Shung, “High-frequency (>50 MHz) medical ultrasound linear arrays fabricated from micromachined bulk PZT materials,” *IEEE Trans. Ultrason. Ferroelectr. Freq. Control*, vol. 59, no. 2, pp. 315–318, 2012.
- [97] N. E. Cabrera-munoz *et al.*, “Forward-looking 30-MHz phased-array transducer for peripheral intravascular imaging,” *Sensors Actuators A Phys.*, vol. 280, pp. 145–163, 2018.
- [98] L. L. P. Wong, A. I. Chen, A. S. Logan, and J. T. W. Yeow, “An FPGA-based ultrasound imaging system using capacitive micromachined ultrasonic transducers,” *IEEE Trans. Ultrason. Ferroelectr. Freq. Control*, vol. 59, no. 7, pp. 1513–1520, 2012.
- [99] B. T. Khuri-Yakub and Ö. Oralkan, “Capacitive micromachined ultrasonic transducers for medical imaging and therapy,” *J. Micromechanics Microengineering*, vol. 21, no. 5, pp. 54004–54014, 2011.
- [100] Arif S. Ergun, G. G. Yaralioglu, and B. T. Khuri-Yakub, “Capacitive Micromachined Ultrasonic Transducers: Theory and Technology,” *J. Aerosp. Eng.*, vol. 16, no. 2, pp. 765–773, 2003.
- [101] K. Brenner, A. S. Ergun, K. Firouzi, and M. F. Rasmussen, “Advances in Capacitive Micromachined Ultrasonic Transducers,” *Micromachines*, vol. 10, no. 2, pp. 1–27, 2019.
- [102] M. I. Haller and B. T. Khuri-Yakub, “A Surface Micromachined Electrostatic Ultrasonic Air Transducer,” in *IEEE Ultrasonics Symposium*, 1994, pp. 1241–1244.

- [103] H. S. Yoon *et al.*, “A 1-MHz 2-D CMUT array for HIFU thermal ablation,” in *AIP Conference Proceedings*, 2017, vol. 1821.
- [104] S. H. Wong, M. Kupnik, K. Butts-Pauly, and B. T. Khuri-Yakub, “Advantages of Capacitive Micromachined Ultrasonics Transducers (CMUTs) for High Intensity Focused Ultrasound (HIFU),” in *IEEE Ultrasonics Symposium*, 2007, pp. 1313–1316.
- [105] A. I. H. Chen, L. L. Wong, A. S. Logan, and J. T. W. Yeow, “A CMUT-based real-time volumetric ultrasound imaging system with row-column addressing,” in *IEEE International Ultrasonics Symposium (IUS)*, 2011, pp. 1755–1758.
- [106] J. Lim, C. Tekes, F. L. Degertekin, and M. Ghovanloo, “Towards a Reduced-Wire Interface for CMUT-Based Intravascular Ultrasound Imaging Systems,” *IEEE Trans. Biomed. Circuits Syst.*, vol. 11, no. 2, pp. 400–410, 2017.
- [107] D. T. Yeh, O. Oralkan, A. S. Ergun, X. Zhuang, I. O. Wygant, and B. T. Khuri-Yakub, “High-frequency CMUT arrays for high-resolution medical imaging,” in *IEEE Ultrasonics Symposium*, 2004, pp. 339–402.
- [108] A. I. Chen, L. L. P. Wong, S. Na, Z. Li, M. Macecek, and J. T. W. Yeow, “Fabrication of a Curved Row – Column Addressed Capacitive Micromachined Ultrasonic Transducer Array,” *J. Microelectromechanical Syst.*, vol. 25, no. 4, pp. 675–682, 2016.
- [109] A. S. Logan, L. L. P. Wong, and J. T. W. Yeow, “A 1-D Capacitive Micromachined Ultrasonic Transducer Imaging Array Fabricated With a Silicon-Nitride-Based Fusion Process,” *IEEE/ASME Trans. MECHATRONICS*, vol. 16, no. 5, pp. 861–865, 2011.
- [110] Z. Zheng, Y. Yao, Y. Sun, and J. T. W. Yeow, “Development of a highly sensitive humidity sensor based on the capacitive micromachined ultrasonic transducer,” *Sensors Actuators B. Chem.*, vol. 286, pp. 39–45, 2019.
- [111] Z. Zheng, Y. Yao, J. A. Liu, Y. Sun, and J. T. W. Yeow, “Highly sensitive CMUT-based humidity sensors built with nitride-to-oxide wafer bonding technology,” *Sensors Actuators B. Chem.*, vol. 294, pp. 123–131, 2019.
- [112] T. Takezaki, M. Kawano, S. Machida, and D. Ryuzaki, “Improvement in lateral resolution of through-transmission scanning acoustic tomography using capacitive micromachined

- ultrasound transducer,” *Microelectron. Reliab.*, vol. 93, no. October 2018, pp. 22–28, 2019.
- [113] M. Maadi, B. Greenlay, C. Ceroici, and R. J. Zemp, “Multi-Frequency CMUT Imaging Arrays for Multi-Scale Imaging and Imaging-Therapy Applications,” in *IEEE International Ultrasonics Symposium (IUS)*, 2017.
 - [114] B. Yin, D. Xing, Y. Wang, Y. Zeng, Y. Tan, and Q. Chen, “Fast photoacoustic imaging system based on 320-element linear transducer array,” *Phys. Med. Biol.*, vol. 49, pp. 1339–1346, 2004.
 - [115] A. P. Jathoul *et al.*, “Deep in vivo photoacoustic imaging of mammalian tissues using a tyrosinase-based genetic reporter,” *Nat. Photonics*, vol. 9, no. April, pp. 239–246, 2015.
 - [116] E. Zhang, J. Laufer, and P. Beard, “Backward-mode multiwavelength photoacoustic scanner using a planar Fabry-Perot polymer film ultrasound sensor for high-resolution three-dimensional imaging of biological tissues,” *Appl. Opt.*, vol. 47, no. 4, p. 561, 2008.
 - [117] C. Zhang, T. Ling, S. Chen, and L. J. Guo, “Ultrabroad Bandwidth and Highly Sensitive Optical Ultrasonic Detector for Photoacoustic Imaging,” *ACS Photonics*, vol. 1, no. 11, p. 1093–1098, 2014.
 - [118] B. D. Lindsey, J. Kim, P. A. Dayton, and X. Jiang, “Dual-Frequency Piezoelectric Endoscopic Transducer for Imaging Vascular Invasion in Pancreatic Cancer,” *IEEE Trans. Ultrason. Ferroelectr. Freq. Control*, vol. 64, no. 7, pp. 1078–1086, 2017.
 - [119] X. Wang, Y. Pang, G. Ku, X. Xie, G. Stoica, and L. V Wang, “Noninvasive laser-induced photoacoustic tomography for structural and functional in vivo imaging of the brain,” *Nat. Biotechnol.*, vol. 21, no. 7, pp. 803–806, 2003.
 - [120] Y. Asao *et al.*, “Photoacoustic mammography capable of simultaneously acquiring photoacoustic and ultrasound images simultaneously acquiring photoacoustic,” *J. Biomed. Opt.*, vol. 21, no. 11, pp. 116009–116009, 2016.
 - [121] C. Tian *et al.*, “Non-Contact Photoacoustic Imaging Using a Commercial Heterodyne Interferometer,” *IEEE Sens. J.*, vol. 16, no. 23, pp. 8381–8388, 2016.
 - [122] J. Lu, Y. Gao, Z. Ma, H. Zhou, R. K. Wang, and Y. Wang, “In vivo photoacoustic imaging of blood vessels using a homodyne interferometer with zero-crossing triggering using a

- homodyne interferometer with zero-crossing,” *J. Biomed. Opt.*, vol. 22, no. 3, 2017.
- [123] A. Hochreiner, J. Bauer-marschallinger, P. Burgholzer, B. Jakoby, and T. Berer, “Non-contact photoacoustic imaging using a fiber based interferometer with optical amplification,” *Biomed. Opt. Express*, vol. 4, no. 11, pp. 4151–4153, 2013.
 - [124] K. L. BELL, P. HAJIREZA, and R. J. ZEMP, “Coherence-gated photoacoustic remote sensing microscopy,” *Opt. Express*, vol. 26, no. 18, pp. 23689–23704, 2018.
 - [125] Z. Zheng *et al.*, “Development of a Novel CMUT-Based Concentric Dual-Element Ultrasonic Transducer: Design, Fabrication, and Characterization,” *J. Microelectromechanical Syst.*, vol. 27, no. 3, pp. 538–546, 2018.
 - [126] O. Oralkan *et al.*, “Capacitive Micromachined Ultrasonic Transducers: Next-Generation Arrays for Acoustic Imaging?,” *IEEE Trans. Ultrason. Ferroelectr. Freq. Control*, vol. 49, pp. 1596–1610, 2002.
 - [127] H. J. Bingzhang Chen, Futong Chu, Xingzhao Liu, Yanrong Li, Jian Rong, “AlN-based piezoelectric micromachined ultrasonic transducer for photoacoustic imaging,” *Appl. Phys. Lett.*, vol. 103, pp. 1–4, 2013.
 - [128] W. Liao *et al.*, “Piezoelectric micromachined ultrasound transducer array for photoacoustic imaging,” in *2013 Transducers & Eurosensors XXVII: The 17th International Conference on Solid-State Sensors, Actuators and Microsystems (TRANSDUCERS & EUROSENSORS XXVII)*, 2013, pp. 1831–1834.
 - [129] Y. Qiu *et al.*, “Piezoelectric Micromachined Ultrasound Transducer (PMUT) Arrays for Integrated Sensing, Actuation and Imaging,” *Sensors (Switzerland)*, vol. 15, pp. 8020–8041, 2015.
 - [130] Z. Zheng, “Capacitive Micromachined Ultrasonic Transducers (CMUTs) for Humidity Sensing,” 2019.
 - [131] K. K. Park, H. J. Lee, M. Kupnik, Ö. Oralkan, and B. T. Khuri-Yakub, “Fabricating Capacitive Micromachined Ultrasonic Transducers With Wafer-Bonding Technology,” in *Proceedings of the IEEE International Conference on Micro Electro Mechanical Systems (MEMS)*, 2008, vol. 12, no. 2, pp. 339–342.

- [132] Y. Matsumoto *et al.*, “Visualising peripheral arterioles and venules through high-resolution and large-area photoacoustic imaging,” *Sci. Rep.*, vol. 8, no. 1, pp. 1–11, 2018.
- [133] Y. Huang, E. O. Hæggestrom, X. Zhuang, A. S. Ergun, and B. T. Khuri-yakub, “A Solution to the Charging Problems in Capacitive Micromachined Ultrasonic Transducers,” *IEEE Trans. Ultrason. Ferroelectr. Freq. Control*, vol. 52, no. 4, pp. 578–580, 2005.
- [134] M. Kupnik, A. S. Ergun, Y. Huang, and B. T. Khuri-yakub, “Extended Insulation Layer Structure for CMUTs,” in *IEEE International Ultrasonics Symposium (IUS)*, 2007, vol. 1, pp. 511–514.
- [135] S. Machida, T. Takezaki, T. Kobayashi, T. Nagata, and H. Tanaka, “Highly Reliable CMUT Cell Structure with Reduced Dielectric Charging Effect,” in *IEEE International Ultrasonics Symposium (IUS)*, 2015, pp. 1–4.
- [136] B. Bayram *et al.*, “Finite Element Modeling and Experimental Characterization of Crosstalk in 1-D CMUT Arrays,” *IEEE Trans. Ultrason. Ferroelectr. Freq. Control*, vol. 54, no. 2, pp. 418–430, 2007.
- [137] S. Zhou and J. A. Hossack, “Reducing Inter-Element Acoustic Crosstalk in Capacitive Micromachined Ultrasound Transducers,” *IEEE Trans. Ultrason. Ferroelectr. Freq. Control*, vol. 54, no. 6, pp. 1217–1228, 2007.
- [138] D. Pang and C. Chang, “Development of a Novel Transparent Flexible Capacitive Micromachined Ultrasonic Transducer,” *Sensors (Switzerland)*, vol. 17, no. 6, 2017.
- [139] X. Zhuang, D. Lin, Ö. Oralkan, and B. T. Khuri-yakub, “Fabrication of Flexible Transducer Arrays With Through-Wafer Electrical Interconnects Based on Trench Refilling With PDMS,” *J. Microelectromechanical Syst.*, vol. 17, no. 2, pp. 446–452, 2008.